

WRDC-TR-89-411 7

**AD-A225 268**

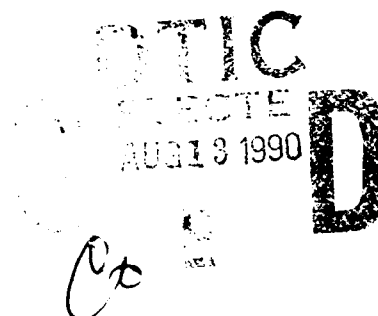
**NUCLEAR MAGNETIC RESONANCE  
NONDESTRUCTIVE EVALUATION  
OF COMPOSITE MATERIALS**

A. C. Lind  
C. G. Fry

McDonnell Douglas Research Laboratories  
St. Louis, Missouri 63166-0516



9 April 1990  
Final Technical Report for the Period  
19 September 1987 — 19 June 1989



Approved for public release; distribution unlimited

Materials Laboratory  
Wright Research Development Center  
Air Force Systems Command  
Wright-Patterson Air Force Base, OH 45433-6533

## NOTICE

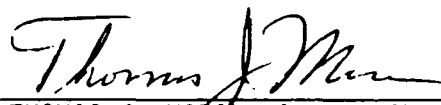
When Government drawings, specifications, or other data are used for any purpose other than in connection with a definitely Government-related procurement, the United States Government incurs no responsibility or any obligation whatsoever. The fact that the government may have formulated or in any way supplied the said drawings, specifications, or other data, is not to be regarded by implication, or otherwise in any manner construed, as licensing the holder, or any other person or corporation; or as conveying any rights or permission to manufacture, use, or sell any patented invention that may in any way be related thereto.

This report is releasable to the National Technical Information Service (NTIS). At NTIS, it will be available to the general public, including foreign nations.

This technical report has been reviewed and is approved for publication.

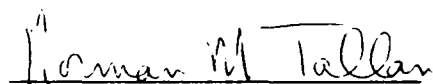


CHARLES F. BUYNAK  
Nondestructive Evaluation Branch  
Metals and Ceramics Division



THOMAS J. MORAN, Acting Chief  
Nondestructive Evaluation Branch  
Metals and Ceramics Division

FOR THE COMMANDER



DR. NORMAN M. TALLAN, Director  
Metals and Ceramics Division  
Materials Laboratory

If your address has changed, if you wish to be removed from our mailing list, or if the addressee is no longer employed by your organization please notify WRDC/MLLP, WPAFB, OH 45433-6533 to help us maintain a current mailing list.

Copies of this report should not be returned unless return is required by security considerations, contractual obligations, or notice on a specific document.

Unclassified

SECURITY CLASSIFICATION OF THIS PAGE

REPORT DOCUMENTATION PAGE				Form Approved OMB No. 0704-0188	
1a. REPORT SECURITY CLASSIFICATION UNCLASSIFIED			1b. RESTRICTIVE MARKINGS		
2a. SECURITY CLASSIFICATION AUTHORITY			3. DISTRIBUTION/AVAILABILITY OF REPORT Approved for public release; distribution unlimited		
2b. DECLASSIFICATION/DOWNGRADING SCHEDULE					
4. PERFORMING ORGANIZATION REPORT NUMBER(S)  MDC QA035			5. MONITORING ORGANIZATION REPORT NUMBER(S)  WRDC-TR-89-4117		
6a. NAME OF PERFORMING ORGANIZATION McDonnell Douglas Research Laboratories		6b. OFFICE SYMBOL (If applicable)	7a. NAME OF MONITORING ORGANIZATION Materials Laboratory (WRDC/MLLP) WRIGHT Research Development Center		
6c. ADDRESS (City, State, and ZIP Code) P.O. Box 516 St. Louis, MO 63166			7b. ADDRESS (City, State, and ZIP Code) Wright-Patterson Air Force Base OH 45433-6533		
8a. NAME OF FUNDING/SPONSORING ORGANIZATION Department of Air Force		8b. OFFICE SYMBOL (If applicable)	9. PROCUREMENT INSTRUMENT IDENTIFICATION NUMBER  F33615-87-C-5247		
8c. ADDRESS (City, State, and ZIP Code)  Air Force Wright Aeronautical Laboratory Materials Lab/Wright-Patterson, AFB			10. SOURCE OF FUNDING NUMBERS		
			PROGRAM ELEMENT NO. 61101F 62102F	PROJECT NO. ILIR	TASK NO. 02
11. TITLE (Include Security Classification)  Nuclear Magnetic Resonance Nondestructive Evaluation of Composite Materials					
12. PERSONAL AUTHOR(S) Lind, Arthur C. and Fry, Charles G.					
13a. TYPE OF REPORT Final Report		13b. TIME COVERED FROM 870919 TO 890619		14. DATE OF REPORT (Year, Month, Day) 1990 April 9	
15. PAGE COUNT 79					
16. SUPPLEMENTARY NOTATION					
17. COSATI CODES			18. SUBJECT TERMS (Continue on reverse if necessary and identify by block number) Nuclear Magnetic Resonance Test Methods Nondestructive Evaluation		
FIELD	GROUP	SUB-GROUP			
20	05	00			
14	02	00			
19. ABSTRACT (Continue on reverse if necessary and identify by block number) Nuclear magnetic resonance (NMR) was studied for use in the nondestructive evaluation of composite materials, with particular emphasis on NMR imaging. NMR parameters of potential use for generating images showing high contrast between acceptable and unacceptable regions of composites were measured for typical organic matrix materials. The attenuating effects of carbon fibers were measured and relationships were developed to compute the conditions necessary to obtain images of carbon-fiber composites. NMR images of aerospace composites containing poly(aryl-ether-ether-ketone) (PEEK) and epoxy resins were obtained using solid state <sup>13</sup> C techniques. The contrast mechanism used for these images was the chemical shift, so that the images revealed the detailed chemical composition of the composites. NMR images of hydrogen in PEEK were also obtained using multiple-pulse techniques to reduce dipolar broadening. Selective pulses were used to obtain images of the spatial variations in the crystalline content of PEEK. The results of these experiments were used to assess the feasibility of using NMR for nondestructive evaluation of composite materials.					
20. DISTRIBUTION/AVAILABILITY OF ABSTRACT <input checked="" type="checkbox"/> UNCLASSIFIED/UNLIMITED <input checked="" type="checkbox"/> SAME AS RPT. <input type="checkbox"/> DTIC USERS			21. ABSTRACT SECURITY CLASSIFICATION Unclassified		
22a. NAME OF RESPONSIBLE INDIVIDUAL Joseph A. Moyzis			22b. TELEPHONE (Include Area Code) (513) 255-9799		22c. OFFICE SYMBOL WRDC/MLLP

DD Form 1473, JUN 86

Previous editions are obsolete.

SECURITY CLASSIFICATION OF THIS PAGE

Unclassified

# FOREWORD

This Final Technical Report covers work performed on Contract No. F33615-87-C-5247 entitled "Nuclear Magnetic Resonance Nondestructive Evaluation of Composite Materials." This program is sponsored by the Wright Research and Development Center, Materials Laboratory, Wright-Patterson AFB, Ohio. Dr. Joseph A. Moyzis is the Project Engineer. Dr. Arthur C. Lind is the Program Manager, and Drs. Arthur C. Lind and Charles G. Fry are Co-Principal Investigators.

Accession For	
NTIS GRA&I	<input checked="" type="checkbox"/>
DTIC TAB	<input type="checkbox"/>
Unannounced	<input type="checkbox"/>
Justification	
By	
Distribution/	
Availability Codes	
Dist	Avail and/or Special
A-1	



## TABLE OF CONTENTS

Section	Page
1.0 SUMMARY.....	1
2.0 INTRODUCTION.....	3
2.1 Program Objectives.....	3
2.2 Program Approach.....	3
2.3 Technical Review and Introduction.....	3
3.0 PROGRESS.....	8
3.1 Composite Samples.....	8
3.2 Contrast Mechanisms.....	9
3.3 $^{29}\text{Si}$ NMR Imaging Considerations.....	11
3.4 Effects of Conducting Carbon Fibers on NMR and NMR Imaging of Composite Materials.....	12
3.4.1 Approximate Analysis.....	13
3.4.2 Carbon-Fiber Samples.....	17
3.4.3 Network Analyzer Measurements.....	18
3.4.4 Nonimaging NMR Measurements.....	20
3.4.5 NMR Imaging Measurements.....	23
3.4.6 Discussion.....	28
3.5 $^{129}\text{Xe}$ and Liquid/Vapor Sorption Experiments.....	34
3.6 $^{13}\text{C}$ NMR Line-Narrowing and Imaging Studies.....	36
3.7 $^1\text{H}$ NMR Line-Narrowing and Imaging Studies.....	48
4.0 ASSESSMENT OF NMR AND NMR IMAGING FOR THE NONDESTRUCTIVE EVALUATION OF COMPOSITE MATERIALS.....	55
REFERENCES.....	62

## LIST OF ILLUSTRATIONS

Figure		Page
1.	Schematic of an NMR imaging experiment.....	5
2.	Nominal and multiple-pulse narrowed $^1\text{H}$ linewidths in solids..	6
3.	Cylinder/piston fixture for crushing composite samples.....	9
4.	Multi-ply carbon-fiber composite.....	14
5.	Coaxial and coplanar coil configurations.....	18
6.	Carbon-fiber composite NMR samples used.....	21
7.	NMR imaging experiment pulse sequence.....	25
8.	Measured attenuation of the RF magnetic field in a cross-ply panel with propagation along $\theta=90^\circ, \phi=0^\circ$ .....	26
9.	Measured attenuation of the RF magnetic field in a cross-ply panel with propagation along $\phi=90^\circ$ .....	28
10.	The transmitter power required in a cross-ply panel with propagation along $\theta=90^\circ, \phi=0^\circ$ .....	30
11.	The relative signal-to-noise in a cross-ply panel with propagation along $\theta=90^\circ, \phi=0^\circ$ .....	32
12.	The transmitter power required to generate a 5- $\mu\text{s}$ , 90-degree rotation in a cross-ply panel with propagation along $\phi=90^\circ$ ...	33
13.	The relative signal-to-noise in a cross-ply panel with propagation along $\phi=90^\circ$ .....	34
14.	$^{129}\text{Xe}$ NMR spectrum of sample (3).....	35
15.	Calibration of the magnetic field gradient.....	37
16.	Schematic of the pulse sequence used to obtain $^{13}\text{C}$ NMR chemical-shift images.....	38
17.	Schematic of the pulse sequence used to obtain $^{13}\text{C}$ NMR images using $^1\text{H}$ spin-lattice relaxation as the contrast mechanism...	38
18.	$^{13}\text{C}$ CP/MAS spectra taken at 7.0 T.....	39
19.	$^{13}\text{C}$ CP/MAS spectra with a selective $3\pi/2$ pulse applied.....	40

LIST OF ILLUSTRATIONS  
(continued)

Figure		Page
20.	$^{13}\text{C}$ chemical-shift image of a DER/DETA resin/Teflon/PEEK resin sandwich.....	45
21.	$^{13}\text{C}$ chemical-shift image of an AS-4/3501-6 laminate/Teflon/PEEK laminate sandwich.....	45
22.	$^{13}\text{C}$ NMR image of a PEEK resin/DER/DETA resin/PEEK resin sandwich.....	46
23.	Schematic of a $^1\text{H}$ NMR imaging experiment.....	52
24.	$^1\text{H}$ NMR images of PEEK sections.....	53
25.	Ratio of volume of $\sim 0\%$ to $26\%$ crystalline PEEK regions.....	53
26.	The RF pulse rotation angle as a function of depth.....	58
27.	The relative signal-to-noise including Q and $T_1$ dependencies.	59

## LIST OF TABLES

Table	Page
1. Issues dominating the last half of the work period.....	7
2. Through-transmission ultrasonic C-scan results.....	8
3. Significance of NMR parameters.....	10
4. Measured NMR parameters of possible use as contrast mechanisms	11
5. <sup>1</sup> H spin-lattice relaxation times of organic resin materials..	12
6. Network analyzer RF attenuation results.....	19
7. Nonimaging NMR RF attenuation results.....	23
8. Summary of predicted and measured values of electrical conductivities for carbon-fiber composites.....	29
9. Estimates of experimental times needed.....	40
10. Sweep widths obtainable from multiple-pulse sequences.....	50



## GLOSSARY OF ACRONYMS AND SYMBOLS

<u>Term</u>	<u>Explanation</u>
A	RF amplitude factor
APC-II	ICI Americas PEEK laminate
B <sub>1</sub>	RF magnetic induction (webers)
BR-24	Burum-Rhim 24-pulse sequence
BR-52	Burum-Rhim 52-pulse sequence
BW	bandwidth (Hz)
c	=1 for a power spectrum, =2 for a magnitude spectrum
CP	cross-polarization
CSU	Colorado State University
d	distance or depth along RF propagation path
DER/DETA	Dow epoxy resin diglycidal-ether of bisphenol-A cured with 2,2'-diaminodiethylamine (diaminodiethyltriamine)
DNCP	dipolar-narrowed Carr-Purcell sequence
DW	dwelt time
f	fiber fraction
FOV	field of view
G	magnetic field gradient (in Tesla/cm)
GE	General Electric Company
G <sub>m</sub>	electrical conductance along m <sup>th</sup> portion of a path
H <sub>0</sub>	static magnetic intensity (ampere-turns/m)
MAS	magic-angle spinning
MDRL	McDonnell Douglas Research Laboratories
MP	multiple pulse
MQ	multiple quantum
MREV-8	Mansfield-Rhim-Ellman-Vaughn 8-pulse sequence
MRI	magnetic resonance imaging - acronym used in hospitals and medical research for NMR imaging; nuclear was dropped for public relation reasons. We use "NMR imaging" in reference to materials studies similar to the work performed in this contract

# GLOSSARY OF ACRONYMS AND SYMBOLS

(Continued)

N	number of plies
NDE	nondestructive evaluation
NMR	nuclear magnetic resonance
OMC	organic matrix/carbon-fiber composites
P	RF power per unit surface area (watts/m <sup>2</sup> )
P <sub>s</sub>	RF power at surface
P <sub>t</sub>	RF power at transmitter
PEEK	poly(aryl-ether-ether-ketone)
PVC	poly(vinyl chloride)
Q	quality factor of probe or RF circuit
R	effective surface area
RF	radio frequency
S( $\alpha$ )	intrinsic line shape
S'( $\nu$ )	measured (truncation-modified) line shape
S <sup>t</sup> ( $\nu$ )	truncation line shape function
S/N	experimental signal-to-noise
SQUID	Superconducting quantum interference devices
SW	sweep width
T	truncation or acquisition time
t <sub>1</sub>	time during evolution period of a two-dimensional or imaging NMR experiment
T <sub>1</sub>	nuclear spin-lattice relaxation time
T <sub>1<math>\rho</math></sub>	nuclear spin-lattice relaxation time in the rotating frame
t <sub>2</sub>	time during the detection period of a two-dimensional or imaging NMR experiment
T <sub>2</sub>	nuclear spin-spin relaxation time observed in a free-induction decay
T <sub>2</sub> <sup>†</sup>	nuclear spin-spin relaxation time during dipole-dipole decoupling
T <sub>CH</sub>	cross-relaxation time between <sup>13</sup> C and <sup>1</sup> H

# GLOSSARY OF ACRONYMS AND SYMBOLS

(Continued)

$t_r$	response time of a circuit
TE	total time for an experiment
$\alpha_1$	angle of carbon fibers in $i^{\text{th}}$ ply
$\gamma$	magnetogyric ratio
$\gamma G$	magnetic field gradient (in Hz/cm)
$\delta$	skin-depth
$\Delta F_{MP}$	frequency interval over which multiple pulse decoupling is effective
$\Delta x$	spatial resolution
$\Delta \nu$	full linewidth at half-height
$\epsilon$	permittivity
$\epsilon_0$	permittivity of free space
$\theta$	pulse rotation angle
$(\theta, \phi)$	direction of RF propagation or electrical conductivity path
$\mu$	magnetic permeability
$\mu_0$	magnetic permeability of free space
$\nu$	RF (Larmor) frequency
$\nu_0$	carrier or centerband RF (Larmor) frequency
$\nu_{1/2}$	intrinsic half-linewidth at half-height
$\nu_{1/2}^E$	half-linewidth of half-height of truncation function
$\nu_{1/2}'$	measured (truncation-modified) half-linewidth at half-height
$\rho$	xenon gas density
$\sigma$	electrical conductivity
$\sigma(90^\circ, 0^\circ)$	electrical conductivity perpendicular to ply direction
$\sigma(\theta, 90^\circ)$	electrical conductivity parallel to ply direction
$\sigma_{  }$	electrical conductivity parallel to length of carbon fiber
$\sigma_{\perp ip}$	effective electrical conductivity perpendicular to length of carbon fibers within the $i^{\text{th}}$ ply
$\sigma_{\perp i, i+1}$	effective electrical conductivity perpendicular to length of carbon fibers going from $i$ to $i+1$ ply
$\tau$	pulse length

## GLOSSARY OF ACRONYMS AND SYMBOLS

(Continued)

$\tau_e$	echo time
$\tau_{90}$	pulse length to obtain 90° rotation of nuclei

## 1.0 SUMMARY

We have made significant progress to evaluate the use of nuclear magnetic resonance (NMR) and NMR imaging for the nondestructive evaluation (NDE) of composite materials. Our accomplishments, including the subsequent publication of two journal articles and portions of a third article, have received considerable attention during presentations at scientific meetings.

NMR imaging of solid-state materials was not well developed at the onset of this contract and specialized equipment and experimental designs were needed for each one of the  $^1\text{H}$ ,  $^{13}\text{C}$ , and  $^{29}\text{Si}$  nuclei. Therefore, we needed to make significant advances to accurately assess the viability of the NMR technique for the NDE of composite systems. The conductivity of the carbon fibers found in the most commonly used aerospace composite systems added yet more complexity to the study. The assessment discussed in Section 4.0 is founded on the following progress achieved during the contract work period:

- i) a quantitative knowledge of the interaction of the conducting carbon fibers with the applied and induced radio-frequency electromagnetic radiation,
- ii) the demonstration of  $^{13}\text{C}$  NMR imaging of aerospace materials, followed by an assessment of signal-to-noise and spatial resolution considerations of  $^{13}\text{C}$  NMR imaging of solids, and
- iii) the design and implementation of a  $^1\text{H}$  NMR imaging experiment, followed by an assessment of the technical advances still needed to be achieved and of other possible approaches to  $^1\text{H}$  NMR imaging of solids.

Evaluation and planning for NMR and NMR imaging of composite materials require a clear, basic understanding of the physics of the interaction of the radio-frequency (RF) electromagnetic fields with the conducting carbon fibers commonly used in aerospace composite systems. The major technical accomplishment of this contract work is the quantitative determination of the RF attenuation caused by the conducting carbon fibers. Without this knowledge, the evaluation and assessment summarized in Section 4.0 would be much more difficult and very likely inaccurate. Determination of contrast mechanisms that are capable of specifically mapping "poor" or flawed regions of carbon-fiber composite systems must await the development of a low-field NMR instrument capable of observing the NMR signals within a carbon-fiber

cross-ply laminate. One possible design for such an instrument is presented in Section 4.0.

A careful assessment of signal-to-noise and spatial-resolution issues for  $^1\text{H}$  and  $^{13}\text{C}$  NMR imaging of solids is presented.  $^1\text{H}$  NMR imaging of solid materials is a viable technique capable of obtaining sub-100- $\mu\text{m}$  spatial resolution. A  $^1\text{H}$  NMR imaging experiment designed under this contract combines an optimum line-narrowing scheme, fast gradient switching, and some aspects of a common liquids magnetic resonance imaging (MRI) experiment to produce good-quality  $^1\text{H}$  images of neat aerospace resin systems. Possible modifications to this experiment are discussed, along with the several technical advances still needing to be achieved before  $^1\text{H}$  NMR imaging of solid materials can become a truly practical technique.  $^{13}\text{C}$  NMR imaging of solid materials is also demonstrated to be a viable technique, but signal-to-noise issues are shown to most likely limit three-dimensional imaging resolutions to greater than 100  $\mu\text{m}$ .

NMR imaging techniques are proving valuable for the NDE of ceramic systems. The direct observation of  $^{29}\text{Si}$  in ceramics, however, is not a viable technique. Current NMR imaging of ceramics relies to a large extent on the use of invasive fluids. The use of  $^{129}\text{Xe}$  (and  $^{13}\text{CO}_2$ ) as an invasive fluid is not useful in NMR imaging for the NDE of organic-matrix composite materials.

## 2.0 INTRODUCTION

### 2.1 Program Objectives

The objective of this program is to investigate the use of the nuclear magnetic resonance (NMR) technique for the inspection and evaluation of composite materials. The emphasis is to evaluate the utility of the NMR technique in determining nuclear-level information in polymeric and ceramic materials that can be linked to macroscopic material properties, with particular focus on the imaging capabilities of NMR in these materials.

### 2.2 Program Approach

This program is being conducted in four tasks:

Task I - Investigate the NMR of  $^1\text{H}$  and  $^{13}\text{C}$  nuclei in organic-matrix composites, such as Graphite/Epoxy or Graphite/PMR.

Task II - Investigate, based on the results of Task I, the ability to image the internal structure and chemistry of organic-matrix composite materials.

Task III - Investigate the potential of using  $^{29}\text{Si}$  NMR for the evaluation of the internal structure of silicon nitride ceramic materials.

Task IV - From the results of Tasks I, II, and III, assess the potential of using NMR and NMR imaging as standard inspection techniques in composite materials of interest to the aerospace community.

### 2.3 Technical Review and Introduction

To perform the nondestructive evaluation (NDE) of organic-matrix/carbon-fiber composites (OMC) by use of nuclear magnetic resonance (NMR) and NMR imaging, we must combine the most demanding aspects of solid-state NMR techniques with a broad knowledge of the physical and chemical characteristics of the material which affect the behavior of the nuclear magnetization. We have endeavored, therefore, to combine the knowledge and experience of other workers in NMR imaging of solid materials with our own unique expertise. In addition to the work performed at McDonnell Douglas Research Laboratories (MDRL), we have made appropriate use of two facilities external to MDRL. The facility at General Electric in Fremont, CA provided primarily a large magnet gap which enabled the assessment of the RF attenuation effects of (relatively) large composite pieces containing long carbon

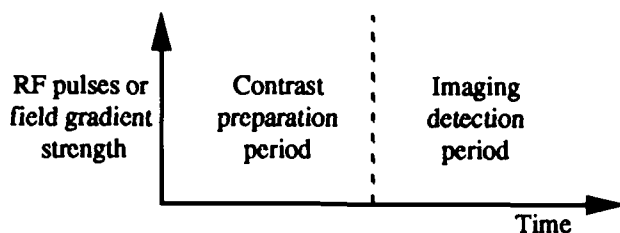
fibers; this work is presented in Section 3.4 (Ref. 1). The facility at Prof. G. Maciel's laboratory at Colorado State University in Fort Collins, CO provided expertise and equipment capable of assessing  $^{13}\text{C}$  NMR imaging of solid materials, as described in Section 3.6 (Refs. 2-4).

Other workers in the field are contributing to the rapid advances which make solid-state NMR imaging a promising new technology. Work involving discussions of NMR as a diffraction technique (Refs. 5,6), selective imaging (Refs. 7,8), multiple-quantum imaging (Refs. 9,10), imaging of quadrupolar nuclei (Refs. 11,12), stepped gradient imaging (Ref. 13), imaging by use of magic-angle narrowing (Refs. 14,15), imaging combining multiple pulse with RF field gradients (Ref. 16), and imaging by use of solid-echoes (Ref. 17) complement the work more similar to nominal magnetic resonance imaging (MRI) of mobile systems involving sorbed fluids in organic polymer systems (Refs. 18-21) and ceramic composites (Refs. 22-26). In the field of NMR imaging of truly solid materials, the Naval Research Laboratories has made (Refs. 27-31) and is continuing to make (Refs. 32,33) significant progress. Recently, a review of NMR imaging in materials science (Ref. 34), the announcement of significant technology advances in NMR microscopy (to  $\sim 10\text{-}\mu\text{m}$  resolutions; Refs. 35,36), and the recent publications of NMR imaging of elastomers (Ref. 37) and high-resolution NMR imaging of solids (Refs. 38-44) display the rapid advances still occurring in the field. The work presented in this report--much of which is either in preparation (Ref. 45), submitted (Ref. 1) or accepted for publication (Ref. 2) and has been presented at technical presentations (Ref. 46)--is up-to-date with the current state of the art in the field. The assessment of the technology as applied to the NDE of OMC and ceramic composite materials presented in Section 4.0 is therefore as up-to-date and accurate as possible.

As described in our proposal, the technology involved in this project can be divided into two phases or periods of the NMR experiment, as shown schematically in Figure 1. First, a suitable contrasting mechanism must be found, such as a relaxation or frequency shift parameter that is useful for contrasting one region of interest in a sample to other regions; otherwise, the imaging detection period will be void of information. The contrast preparation period is amenable to traditional NMR techniques (Refs. 47-49) applied to OMC and ceramic composite samples.

The second phase of the technology directly involves imaging aspects of the experiment, the most important of which are sensitivity and spatial





89-221-210a

Figure 1. Schematic of an NMR imaging experiment

resolution. Sensitivity is in some respects determined by the sample itself, and we must remember that NMR is intrinsically an insensitive technique. While the experimental design can be optimized for sensitivity by probe and coil modifications, spatial resolution will often be limited by sensitivity issues since increasing the spatial resolution directly involves reducing the volume element (voxel) being detected. The experimental acquisition time,  $TE$ , varies with the inverse square of the volume element,  $V$ :

$$TE \propto V^{-2} \quad (1)$$

Describing the voxel in terms of all three spatial dimensions, we obtain

$$TE \propto (\Delta x)^{-2} (\Delta y)^{-2} (\Delta z)^{-2} \quad (2)$$

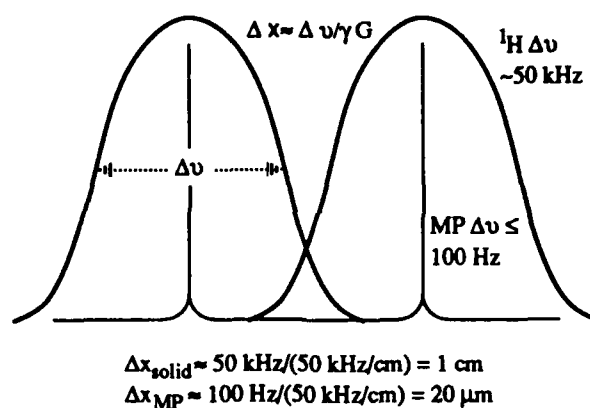
Thus, to double the spatial resolution in each dimension,  $TE$  will be 64 times longer to obtain the same S/N within the voxel. Magnetic resonance imaging of liquids (MRI) is currently (and will probably remain) limited in resolution due to sensitivity issues (Ref. 50). We will show in Section 3.6 that the resolution of  $^{13}\text{C}$  images of solids are currently limited by sensitivity. To obtain adequate resolution, the experiment must continue long enough to acquire sufficient S/N. Since current  $^{13}\text{C}$  NMR imaging experiments take about an hour to acquire a one-dimensional image, doubling resolutions or adding other dimensions in the image quickly becomes unrealizable.

Moreover, in solid materials, obtaining adequate spatial resolution requires the use of line-narrowing techniques or extremely large gradients in the magnetic field strength. The relationship between spatial resolution  $\Delta x$  in cm, the linewidth  $\Delta\nu$  in  $\text{s}^{-1}$ , and the magnetic field gradient,  $G$ , in T/cm is

$$\Delta x \approx \Delta\nu / (\gamma G) \quad (3)$$

where  $\gamma$  is the magnetogyric ratio of the nuclei being detected.

The situation in solids is shown in Figure 2, where typical NMR linewidths in solid materials are shown. Sophisticated RF multiple-pulse sequences (denoted by MP in the figure), which complicate the experiment and place restrictions on the sample and probe design, are one approach to achieving better spatial resolution through line narrowing. New gradient designs already allow the application of much larger magnetic field gradients than were available one year ago (up to a factor of 20; Ref. 36), but some line narrowing by use of RF multiple-pulse sequences is still necessary due to limitations in receiver bandwidth and sensitivity issues, as discussed in Section 3.7.



89-221-211a

**Figure 2.** Nominal (~50 kHz) and multiple-pulse narrowed (MP; 100 Hz) hydrogen line widths in solid materials. Spatial resolution ( $\Delta x$ ) is achieved by separating  $^1\text{H}$  lines of different regions from one another in frequency by use of the gradient  $\gamma G$ .  $\Delta x$  is large for nominal solids when using a moderate gradient of 50 kHz/cm, but is greatly improved when MP line-narrowing is used.

At the end of the first half of our work period, three issues were determined as being critical in assessing the feasibility of NMR and NMR imaging for the NDE of OMC. Table 1 briefly describes each issue and summarizes our significant advances with each.

First, sensitivity must be attainable within a reasonable period of time (up to many days). Even with an optimized experimental design, this is not always feasible due to intrinsic characteristics of the material and the

Table 1. Issues dominating the last half of the work period.

Issue	Significant advances
Sensitivity attainable?	<ul style="list-style-type: none"> <li>• No for <math>^{29}\text{Si}</math> in ceramics</li> <li>• No for <math>^{129}\text{Xe}</math> as invasive fluid</li> <li>• Probably for <math>^{13}\text{C}</math> in OMC</li> <li>• Yes for <math>^1\text{H}</math> in OMC</li> </ul>
Effect of carbon fibers	<ul style="list-style-type: none"> <li>• Quantified rf attenuation for propagation both perpendicular and parallel to ply direction</li> </ul>
Technical advances for $^1\text{H}$	<ul style="list-style-type: none"> <li>• Quadrature detection with MP decoupling</li> <li>• Obtained 2D images with standard MRI use of gradients</li> </ul>

89-221-237a

detected nuclei.  $^{29}\text{Si}$  NMR of ceramic materials and use of  $^{129}\text{Xe}$  as an invasive fluid were both found to have excessive sensitivity problems, as discussed in Sections 3.3 and 3.5, respectively. Sensitivity is also an important issue for the feasibility of  $^{13}\text{C}$  NMR imaging of OMC, but we have found that adequate sensitivity might be achieved with appropriate experimental design as shown in Section 3.6.

Second, the effects of the conducting carbon fibers on the RF propagation had to be understood quantitatively before progress toward NDE of large-scale structures could be made. We have quantified these effects, and this issue still dominates any consideration of the NDE of large-scale OMC, as described in Section 3.4.

Third, technical advances, which we specify and have made progress on as described in Section 3.7, must be achieved before  $^1\text{H}$  NMR imaging of solids can become a practical, useful NDE tool. During the last half of our work period, we therefore directed our research to understand and clarify these three areas. The rest of this report will follow our work outline, as detailed in our proposal. The three issues described above, however, will be emphasized. All the work performed led to the assessment of future viability and an experimental design for NMR imaging for the NDE of OMC, as summarized in Section 4.0.

### 3.0 PROGRESS

#### 3.1 Composite Samples

We obtained a series of 26 carbon-fiber composite samples, and the uncured 3501-6 resins used to fabricate them, from McDonnell Aircraft Company. These samples had been fabricated under the USAF Manufacturing Science Program "Computer-Aided Curing of Composites" (Contract No. F33615-83-C-5088). The samples were originally fabricated according to different processing conditions from resins having either zero, one, or two times the normal amount of  $\text{BF}_3$  catalyst. Our samples, cut from larger scraps left over from this program, are 75 mm wide and 7.6 mm thick at one end. Midway along their 600-mm length, the samples taper down to 3.2 mm.

The samples had been subjected to numerous destructive and nondestructive tests. Table 2 specifies the resin properties and processing conditions for the 26 samples and lists the results of their ultrasonic NDE. These samples provide an excellent range of "poor" quality samples in terms of void content and improper curing. "Poor" characteristics of cracking and fiber breakage were simulated by placing samples in the cylinder/piston fixture shown in Figure 3 and hitting the piston with a hammer. The samples and fixture were cooled to 77 K to induce brittle fracture.

Table 2. Through-transmission ultrasonic C-scan results<sup>(1)</sup> for carbon-fiber/epoxy samples.

Batch number Variation $\text{BF}_3$ content (wt%)	1 Low flow 2.2	1 <sup>(2)</sup> Normal flow 1.1	3 High RC 1.1	4 High flow 0	5 <sup>(3)</sup> Normal flow 1.1	6 Vacuum degas 1.1
Baseline laminate	Clean	Clean	Clean	Clean	Clean	Clean
"Wet" prepeg	Moderate porosity	Moderate porosity	Extreme porosity	Gross porosity	Gross porosity	Minor porosity
"Aged" prepeg	Clean	Clean	Clean	Clean	Clean	Clean
No debulking	—	Clean	Clean	—	Clean	Minor porosity
Over bleed	Moderate porosity	Clean	Clean	Minor porosity	—	—

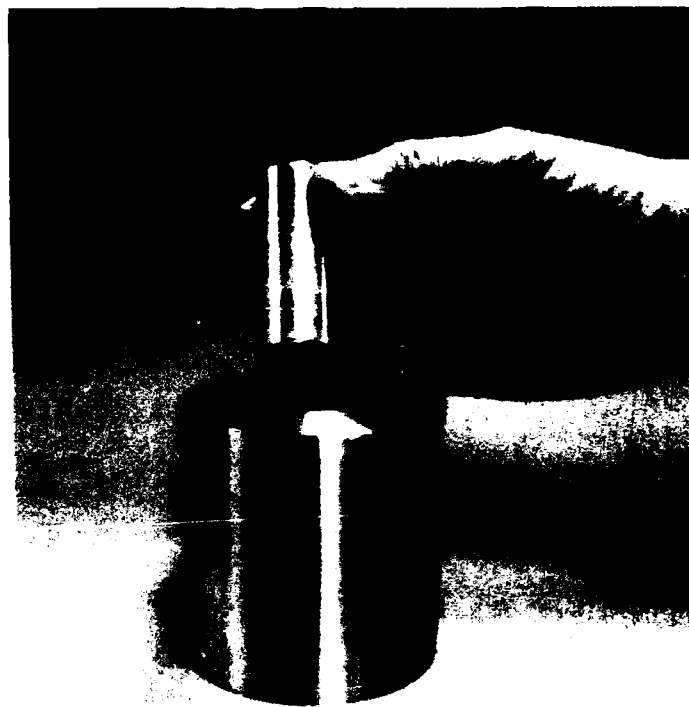
Notes:

(1) Extreme-gross-moderate-minor-clean  
(Bad) (Good)

(2) Control for batches 1, 3, and 4

(3) Control for batch 6

89-221-263



89-221-212

Figure 3. Cylinder/piston fixture for crushing composite samples.

### 3.2 Contrast Mechanisms

At the beginning of our contract work period, we believed that a major portion of the progress would be to determine contrast mechanisms which would allow the detection of poor regions of a material by contrasting them against good regions for use in the NDE of OMC. Although contrast mechanisms remain an important area of study, we have deemphasized this area with respect to the areas of study discussed in Section 2.3. We have obtained some useful observations from this study of contrast mechanisms, as discussed below.

The physical and chemical parameters of significance for possible use as contrast mechanisms are listed in Table 3.  $^{29}\text{Si}$  can be substituted for  $^{13}\text{C}$  in this table, as can any fluid system (e.g.,  $^{13}\text{CO}_2$ ) for  $^{129}\text{Xe}$ , depending on the particular system of interest. With a knowledge of these parameters, we can design an NMR experiment to optimize signal-to-noise and contrasting, and to minimize artifacting.

Table 3. Significance of NMR parameters.

NMR Parameters	Significance
$^1\text{H } T_1$	Sensitive to fast motions, paramagnetic impurities
$^1\text{H } T_2$	Sensitive to motions $\lesssim 10^4$ Hz
$^1\text{H } T_{1\rho}$	Sensitive to slow motions
$^1\text{H } T_2^+$	Defines spatial resolution of $^1\text{H}$ imaging, sensitive to proton coupling
$^1\text{H } T_2^{\text{MW4}}$	Sensitive to slow motion, relatively insensitive to experimental calibration
$^{13}\text{C MAS } \delta$	Determine isotropic chemical shifts
$^{13}\text{C } T_{\text{CH}}$	Defines chemical moiety imaging, depends on number of protons, short range
$^{13}\text{C stat}$	Defines chemical shift imaging, depends on anisotropies
$^{13}\text{C } T_2^+$	Defines spatial resolution of $^{13}\text{C}$ imaging
$^{129}\text{Xe } \delta$	Changes caused by matrix
$^{129}\text{Xe } T_1$	Sensitive to impurities, void sizes
$^{129}\text{Xe } T_2$	Defines spatial resolution of $^{129}\text{Xe}$ imaging

89-221-239a

Parameters for possible use as contrast mechanisms were measured on various relevant OMC samples, as shown in Table 4. Because of the emphasis on issues detailed in Table 1, we used only the basis set of parameters shown in Table 4, which permitted a detailed investigation of those issues. We did observe very different RF attenuation between long carbon fibers and broken fibers, which could possibly be used for contrasting such defects (see Section 3.4.5).  $^1\text{H}$  spin-lattice relaxation times,  $T_1$ , and  $^{13}\text{C}$  chemical shifts were used with  $^{13}\text{C}$  NMR imaging to contrast PEEK from epoxy resin (see Section 3.6), and  $^1\text{H}$  spin-lattice relaxation times in the rotating frame,  $T_{1\rho}$ , were used with  $^1\text{H}$  NMR imaging to contrast crystallinity differences in PEEK (see Section 3.7). We have observed long, spin-spin relaxation,  $T_2$ , due to sorbed water in composite materials, which might be used to quantify and/or image water distributions in OMC. Other researchers have used  $^1\text{H}$  density to image various phenomena in more mobile elastomers (Ref. 37), but these liquid-like experiments are not applicable to the study of solid OMC materials.

Table 4. Measured NMR parameters of possible use as contrast mechanisms.

Parameters	Sample					
	Neat PEEK	Carbon-fiber laminated PEEK	Chopped-carbon-fiber PEEK	Glass-fiber PEEK	Neat 3501-6 resin	AS-4/3501-6 laminate
$^1\text{H } T_1$ (s)	1.0 <sup>1</sup> 1.4 <sup>2</sup>	0.83	0.65	0.90	0.5	2.8
$^1\text{H } T_2$ ( $\mu\text{s}$ )	12	14.2	13.7	13.6	8.1	9.2
$^1\text{H } T_{1\rho}$ (ms)	20 <sup>3</sup> 3 <sup>4</sup>					
$^1\text{H } T_2^{\text{MW4}}$ (ms)	8				13	5
$^1\text{H } T_2^+$ (MP) ( $\mu\text{s}$ )	160				160	
$^1\text{H } T_2^+$ (DNCP) (ms)	1.3				1.1	
$^{13}\text{C MAS}\delta$ (ppm)	115 130 148 155 192				14 109 23 126 37 148 49 67	
$^{13}\text{C } T_{\text{CH}}$ (ms)	16 (115) 15 (130) 18 (148)				alip ~ 0.4 arom ~ 1.5	
$^{13}\text{C } T_2^+$ (ms)	> 6				> 6	

<sup>1</sup> At room temperature

<sup>2</sup> At 403° K

<sup>3</sup> Crystalline

<sup>4</sup> Amorphous

89-221-262a

To conclude, optimizing contrast to clarify flaws and inhomogeneities within OMC must await the development and simultaneous combining of techniques which together will be able to use such contrast information. We demonstrate the feasibility of such combination experiments, within definitive constraints for OMC, and assess the future capabilities of NMR and NMR imaging in Section 4.0.

### 3.3 $^{29}\text{Si}$ NMR Imaging Considerations

For a portion of this contract, we were to investigate  $^{29}\text{Si}$  NMR for imaging composite ceramics containing silicon nitride or other silicon compounds. Unfortunately, the spin-lattice relaxation times,  $T_1$ , in these compounds are very large, often minutes (Ref. 51), whereas they are about one second for hydrogen; see Table 5. Hydrogen in hydrogen-containing

Table 5.  $^1\text{H}$  spin-lattice relaxation times of organic resin materials at room temperature.

Material	$^1\text{H } T_1 (\text{s})$	
	2.3 T	7 T
DER/DETA resin	0.33	0.32
3501-6 resin	2.0	0.5
PEEK XK300 resin	1.4	1.0
PEEK laminate	1.6	0.83
AS-4/3501-6	1.15	2.0

89-221-240a

compounds strongly dipole-dipole couple to each other; so, if only a few hydrogen relax quickly to the lattice, they all relax quickly, substantially shortening hydrogen  $T_1$  values.  $^{29}\text{Si}$ , being a relatively dilute (4.7% natural abundance) isotope, has no such mechanism for rapidly relaxing to impurities. Therefore, the  $^{29}\text{Si } T_1$  values in ceramics which contain no  $^1\text{H}$  nuclei to relax the  $^{29}\text{Si}$  nuclei are determined by the amplitudes of small,  $\sim 10^8$ -Hz motions of the  $^{29}\text{Si}$  nuclei themselves. As a result, the time to produce an NMR image using  $^{29}\text{Si}$  for detection is excessively long.

The total time of a NMR imaging experiment, TE, depends on  $T_1$  as

$$\text{TE} \propto T_1. \quad (4)$$

In protonated systems such OMC, the  $^1\text{H } T_1$  is used in Equation (4) because cross-polarization (CP) between the dilute spins and proton bath is possible. Thus,  $^{13}\text{C}$  can be used for detection in such systems. In ceramic systems, such as SiC, there are no protons to effect CP. Thus, we have not pursued  $^{29}\text{Si}$  NMR for the NDE of ceramics.

### 3.4 Effects of Conducting Carbon Fibers on NMR and NMR Imaging of Composite Materials\*

High-strength, high-stiffness, low-weight, organic-matrix composite materials used in the aerospace industry frequently contain carbon fibers. Carbon fibers are electrically conducting and will therefore attenuate RF magnetic fields. Without proper accounting for this attenuation, NMR images

\* Most of this section is published in Ref. 1.



of carbon-fiber composites will be seriously degraded and interpretations will be either misleading or impossible. NMR images of small carbon-fiber/polymer composites have been reported (Refs. 2,45,52; see also Section 3.6). These images were obtained only because the samples were small, and oriented such that the dimension of the sample along the direction of RF propagation was less than a distance which we quantify here as the skin depth,  $\delta$ , resulting in small RF attenuations. The present study was conducted to determine the conditions necessary to obtain acceptable NMR images of carbon-fiber composites.

A rigorous calculation of the attenuation of the RF magnetic field as it enters an arbitrarily shaped carbon-fiber composite material is difficult. Other workers have performed detailed calculations for dielectrically lossy isotropic materials having cylindrical (Ref. 53) or planar (Ref. 54) shapes. In carbon-fiber composite materials, however, the attenuation results from induced eddy currents rather than dielectric losses (Ref. 55) because of the high electrical conductivities of the fibers. The induced eddy currents, and thus the RF attenuation, depend on the RF frequency, the geometry of the RF coil, the shape of the sample, and the orientation of the carbon fibers and sample relative to the RF coil.

In Section 3.4.1, assumptions are made to permit simple calculations of the approximate RF attenuation in highly conducting anisotropic carbon-fiber composites. The theory is based on the concept of a skin-depth in good conductors having anisotropic electrical conductivities,  $\sigma$ . Three methods were used to measure the electrical conductivities of the composites. First, a network analyzer was used, as is described in Section 3.4.3, to measure  $\sigma$  along the fibers in cross-ply and unidirectional composites, and also to measure  $\sigma$  going from fiber to fiber. Next, we performed similar measurements using nonimaging NMR, as described in Section 3.4.4. Finding both the network analyzer and nonimaging NMR techniques to be sensitive to errors caused by experimental and sample-makeup imperfections, we used NMR imaging to obtain a set of accurate electrical conductivities, as discussed in Section 3.4.5. These measurements confirm the validity of our approximate analysis, as discussed in Section 3.4.6, and allow an accurate assessment of NMR and NMR imaging as applied to carbon-fiber composite materials.

**3.4.1 Approximate Analysis** In an anisotropic material, induced eddy currents arising from an applied RF magnetic field will depend on the values

of the electrical conductivity along each direction of the induced current. Since different portions of the path are connected in series, the induced eddy current will be limited by the smallest values of electrical conductance along the current path:

$$G_{\text{path}} = \left[ \sum_{m=1}^N \frac{1}{g_m} \right]^{-1}, \quad (5)$$

where  $g_m$  is electrical conductance along the  $m^{\text{th}}$  portion of the path. If the conductance is large along the complete path, then the eddy current will be large, and thus also the RF attenuation. If the conductance is small along any significant portion of the path, the eddy currents will be significantly reduced, and RF penetration will be greatly enhanced. Therefore, to achieve optimum NMR imaging conditions, the object to be imaged must be oriented relative to the RF field to minimize the conductance along the current paths, thereby reducing the eddy currents and the resulting RF attenuation.

Figure 4 illustrates the relevant details of a typical multi-ply carbon-fiber composite. For clarity, the details of only the first two plies are shown. The carbon fibers in the  $i^{\text{th}}$  ply lie in the xy-plane and make an angle,  $\alpha_i$ , with the x axis. Generally, the angles,  $\alpha_i$ , repeat every N plies; e.g., a composite structure requiring greatest strength along the x direction might have  $N=2$ ,  $\alpha_1=20^\circ$ , and  $\alpha_2=-20^\circ$ .

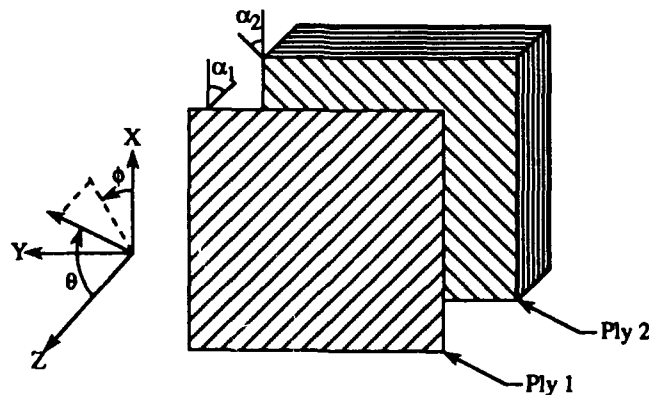


Figure 4. Multi-ply carbon-fiber composite. The first ply is displaced to show the orientation of the fibers in the second ply. The coordinate system used for determining the direction  $(\theta, \phi)$  is also shown.

A reasonable estimate for the electrical conductivity along one particular direction  $(\theta, \phi)$ , as shown in Figure 4, is given by an average of the principal values of the conductivity tensor,  $\sigma$ , of the carbon fibers weighted by the square of the cosine of the angles between the direction  $(\theta, \phi)$  and the principal axes of the conductivity tensor. The result is

$$\begin{aligned} \sigma(\theta, \phi) = & N^{-1} \sin^2 \theta \left[ \sum_{i=1}^N \left[ f \sigma_{||} \cos^2(\phi - \alpha_i) + \sigma_{\perp} \sin^2(\phi - \alpha_i) \right] \right. \\ & \left. + \cos^2 \theta \left[ N^{-1} \sum_{i=1}^N \sigma_{\perp i, i+1}^{-1} \right]^{-1} \right], \end{aligned} \quad (6)$$

where  $f$  is the volume fraction of the carbon fibers,  $\sigma_{||}$  is the electrical conductivity of the carbon fibers along their length, and  $\sigma_{\perp}$  and  $\sigma_{\perp i, i+1}$  are the effective electrical conductivities of the carbon fibers perpendicular to their length, including contact resistance between adjacent fibers, within a ply and from ply  $i$  to ply  $i+1$ , respectively.  $\sigma_{||}$  is an intrinsic property of the carbon fiber while  $\sigma_{\perp}$  and  $\sigma_{\perp i, i+1}$  are extrinsic properties depending upon conditions used to fabricate the composites.

The last two terms in Equation (6) are difficult to estimate. The conductivities  $\sigma_{\perp}$  and  $\sigma_{\perp i, i+1}$  depend upon contact resistance between adjacent fibers which varies because of the different consolidations achieved during fabrication. Moreover, the last term in Equation (6) takes into account that ply-to-ply electrical contacts constitute resistors in series which differ from ply to ply depending upon the difference in the angles between the fibers in the adjacent plies. When the difference in angles between adjacent plies is  $90^\circ$ , the carbon fibers in the adjacent plies come into better electrical contact than when the difference in angles is  $0^\circ$  (i.e., unidirectional).

The electrical conductivity parallel to the fiber axis,  $\sigma_{||}$ , on the other hand, is usually available from the fiber manufacturer or can be obtained by simple measurements (Ref. 56).  $\sigma_{||}$  is orders of magnitude larger than  $\sigma_{\perp}$  and  $\sigma_{\perp i, i+1}$ , and the conductivities perpendicular to the fiber axis can, therefore, usually be neglected in Equation (6). Notable exceptions are cases where the first term in Equation (6) is identically equal to zero.

One such case of importance is the conductivity in a direction normal to the plies, when  $\theta=0^\circ$ ; in this case  $\sigma(0^\circ, \phi) = N[\sigma_{\perp i, i+1}^{-1}]^{-1}$ . Because the conductivity in this direction is relatively small, this case is useful for imaging the interior of carbon-fiber composite materials. Thus, it is important to quantify  $\sigma_{\perp i, i+1}$  and the experiments reported here provide this and related quantities for carbon-fiber composites.

In Section 3.4.6 we show that the conductivity of carbon-fiber/epoxy composites, irrespective of the direction along which the conductivity is measured, is large enough to satisfy the condition

$$\sigma \gg 2\pi\nu\epsilon, \quad (7)$$

where  $\nu$  is the RF frequency and  $\epsilon$  is of the order of the free-space permittivity,  $\epsilon_0 = 8.854 \times 10^{-12}$  F/m. When this condition is satisfied and the dimensions of the composite are much larger than the skin depth

$$\delta = (1/\pi\nu\sigma)^{1/2}, \quad (8)$$

where  $\mu$  is the magnetic permeability, usually equal to that of free space  $\mu_0 = 4\pi \times 10^{-7}$  H/m, then two simplifying approximations can be made which facilitate the calculation of the RF field in the composite (Ref. 57):

- i) treat the object as a superconductor which is impenetrable by the RF magnetic field; i.e., the RF magnetic field at the surface is parallel to the surface, and
- ii) break the surface of the object into small regions that are considered to be planar into which plane electromagnetic waves propagate normal to the surfaces.

Although not done here, the RF magnetic field at the surface can be calculated by solving the corresponding magnetostatic problem for a superconductor of the same size and shape. In this work, estimates of the surface currents are obtained by treating the surface of the object as a mirror; the magnetic (electric) field on the surface is the sum of the applied field and a positive (negative) image field (the image field being a physical expression of the fields arising from the induced eddy currents). The resulting RF magnetic fields lie parallel to the surfaces of the conducting object and they propagate into the object as a plane wave.

The magnetic intensity  $H$  (ampere turns/m) of the plane electromagnetic wave propagating into the conducting media decays exponentially with increasing distance into the sample as

$$H(d) = H_s \exp(-d/\delta), \quad (9)$$

where  $H_s$  is the magnetic intensity at the surface,  $d$  is the distance from the surface along the propagation path. The conductivity of the composite in a direction lying in the plane of the surface and at right angles to the RF magnetic field direction (i.e., in a direction parallel to the RF electric field) is the appropriate electrical conductivity to use in the expression for the skin depth. The RF attenuation (in dB) experienced by a plane wave propagating a distance,  $d$ , is  $8.68 d/\delta$ .

Since the RF transmitter power in solid state experiments is usually very large, it is important to calculate the power required. The RF transmitter is used to rotate the nuclei in the sample about prescribed axes. The faster the rotation, the larger the power required. The magnetic intensity  $H(d)$  required to rotate the nuclei at the location,  $d$ , by  $\theta(d)$  (degrees) during a pulse of duration,  $\tau$ , is given by

$$H(d) = \frac{2}{360} \frac{\theta(d)}{\gamma \tau \mu_0}. \quad (10)$$

The power crossing a unit area ( $W/m^2$ ) at the location  $d$  is given by (Ref. 58)

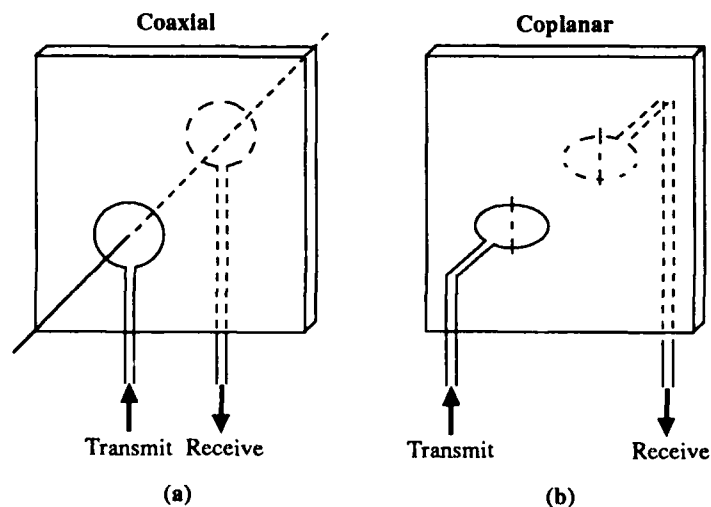
$$P(d) = [H(d)]^2 (\pi \nu \mu_0 / \sigma)^{1/2}. \quad (11)$$

The power crossing a unit area at the surface of the composite sample can be computed using Equation (9), which accounts for the attenuation caused by the carbon-fiber composite.

**3.4.2 Carbon-Fiber Samples** Carbon-fiber/epoxy composite samples were fabricated from AS-4/3501-6 from Hercules, Inc. (Magna, Utah). The conductivity of the fibers,  $\sigma_{||}$ , is about  $7 \times 10^4$  S/m. The samples were cured for one hour at 390 K, followed by curing for three hours at 450 K.

Consolidation of the samples was achieved during cure by either encasing them in a vacuum bag or by applying mechanical pressure; a high-pressure autoclave was not used. From previous measurements (Ref. 59), we estimate that the fiber fraction,  $f$ , was about 0.7.

**3.4.3 Network Analyzer Measurements** The RF attenuation caused by carbon-fiber composite panels having different fiber orientations and thicknesses were measured using a Hewlett Packard HP-8510 network analyzer. The transmit-and-receive portions of the analyzer were connected to single-turn, 2.5-cm-diameter loops placed about 1 cm apart in either a coaxial or coplanar orientation, as shown in Figures 5 (a) and (b), respectively. The loops were electrostatically shielded (Ref. 60) to ensure measurement of only the RF magnetic fields. The frequency was swept between 45 and 300 MHz. The network analyzer was calibrated to measure 0-dB attenuation in the absence of a panel, and the attenuation caused by a carbon-fiber composite panel was measured by placing the panel midway between the coils. Table 6 shows results for 19 x 19-cm cross-ply ( $N=2$ ,  $\alpha_1=0^\circ$ ,  $\alpha_2=90^\circ$ ) and 7 x 7-cm unidirectional ( $N=1$ ,  $\alpha_1=0^\circ$ ) panels.



89-221-214b

Figure 5. Coaxial (a) and coplanar (b) coil configurations used to measure the attenuation of the RF magnetic field caused by carbon-fiber composite panels using a network analyzer.

The results for the cross-ply panels show that the attenuation was greater when the coils were coaxial than when they were coplanar. The RF magnetic fields in the coaxial case tend to be normal to the surface, contrary to the conditions required in the second approximation given above. The RF fields bend upon approaching the surface of the panel in an attempt to become parallel to the surface, but the transmit-and-receive coils can only couple to each other in the coaxial arrangement with the RF magnetic field normal to the surface. Thus, the RF that does propagate through the panel but is parallel to the surface, will not be detected at the receive coil in the coaxial arrangement. The electrical conductivity  $\sigma(90^\circ, \phi)$  for the cross-ply panels was predicted to be 25,000 S/m by use of Equation (6) with  $f=0.7$ ,  $N=2$ ,  $\alpha_1=0^\circ$ ,  $\alpha_2=90^\circ$ ,  $\theta=90^\circ$ ,  $\phi$  arbitrary,  $\sigma_{||}=70,000$  S/m, and neglecting  $\sigma_{\perp}$ . The coplanar incremental amplitudes between the two-ply and four-ply samples given in Table 6 were used in Equation (9) to calculate  $\sigma$ . The result was  $23,000 \pm 12,000$  S/m, in reasonable agreement with the predicted value. Coplanar coils were always used in the following measurements, since this arrangement couples the coils with RF oriented parallel to the surface, which is the primary propagation mode for these samples.

Table 6. Network analyzer RF attenuation results for carbon-fiber composite panels.

Coil configuration/ panel	Thickness	Relative magnetic-field amplitude			
		45 MHz	96 MHz	198 MHz	300 MHz
Coaxial/ 0°, 90° cross-ply, 19 × 19 cm	No panel	1	1	1	1
	2-ply (≈ 0.27 mm)	0.24	0.11	0.045	0.022
	4-ply (≈ 0.53 mm)	0.10	0.045	0.018	0.010
Coplanar/ 0°, 90° cross-ply, 19 × 19 cm	No panel	1	1	1	1
	2-ply (≈ 0.27 mm)	0.40	0.32	0.22	0.13
	4-ply (≈ 0.53 mm)	0.20	0.14	0.079	0.050
	6-ply (≈ 0.80 mm)	0.14	0.079	0.045	0.018
	24-ply (3.2 mm)	*	*	*	*
Coplanar/ unidirectional, electric-field $\perp$ fibers, 7 × 7 cm	No panel	1	1	1	1
	31-ply (4 mm)	0.95	0.88	0.72	0.63
	61-ply (8 mm)	0.94	0.85	0.72	0.60
Coplanar/ unidirectional, electric field $\parallel$ fibers, 7 × 7 cm	No panel	1	1	1	1
	31-ply (4 mm)	0.78	0.53	0.34	0.27
	61-ply (8 mm)	0.68	0.50	0.34	0.28

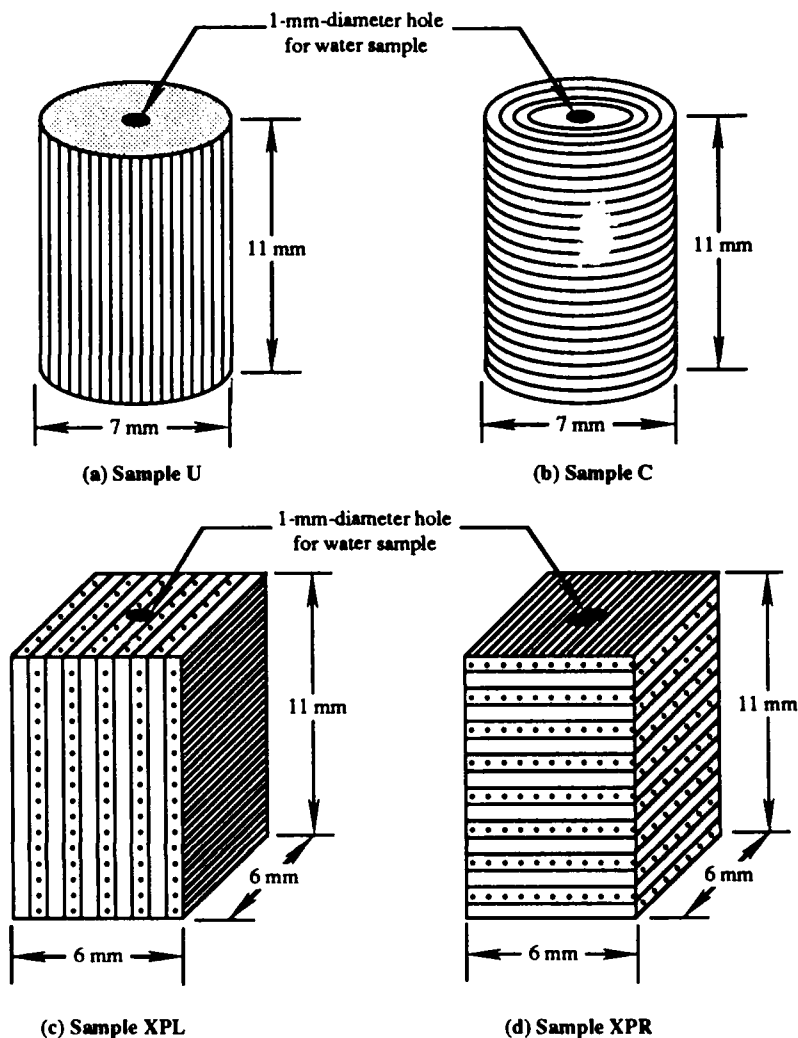
\* Too small to measure;  $< 0.01$ .

89-221-241b

The RF attenuation produced by the unidirectional panels should have been very small for one polarization of the RF magnetic field and very large for the other polarization. The measured results were inconsistent, probably because the small size of the panels allowed the RF fields to go around the edges of the panels, producing an apparent small attenuation. Thus, these results give a lower bound on the attenuation for unidirectional carbon-fiber composites. When the RF magnetic field is applied parallel to the fibers so that the electric field was perpendicular to the fibers ( $\theta=90^\circ$ ,  $\phi=90^\circ$ ), Equation (6) predicts that the conductivity is equal to  $\sigma_{\perp}$ , with the resulting attenuation being small. The measured attenuation was small, as shown in Table 6, and when used in Equation (9) to calculate the effective conductivity, the  $\sigma_{\perp}$  values ranged from 0.3 to 11 S/m. When the RF magnetic field is applied perpendicular to the fiber axes so that the electric field was parallel to the fibers ( $\theta=90^\circ$ ,  $\phi=0^\circ$ ), Equation (6) predicts  $\sigma(90^\circ, 0^\circ) = f\sigma_{||} = 49,000$  S/m, resulting in amplitude factors of 0.00002 or less. Table 6 shows, however, measured values not less than 0.28. The finite size of the panel limits current flow along the fiber, causing the RF to "leak" around the sides of the panel. When the fibers are longer than one-half the RF wavelength, the current can flow without fiber ends interfering, and the leakage problem will be reduced. The lower-than-expected attenuation quite likely is also due to imperfections in the coils and to samples which allowed components of the RF magnetic field to lie in the direction where the attenuation was very small; i.e., alignment of portions of the RF electric field perpendicular to the fiber directions allows the RF to leak through the panel.

**3.4.4 Nonimaging NMR Measurements** Four small, cylindrical, carbon-fiber/epoxy samples were fabricated, as shown in Figure 6, for evaluating the effects of fiber orientation on RF attenuation by use of nonimaging NMR. In all cases, a 1-mm-diameter hole was drilled to a depth a few millimeters beyond the center of the sample to accommodate a capillary tube containing water. The axis of the 1-mm hole was always colinear with the probe solenoidal coil axis in the NMR experiments. Sample U contained unidirectional fibers aligned parallel to the cylinder axis, and sample C contained fibers circumferentially wound about the axis of the cylinder. The consolidation in samples U and C was not as good as normally achieved





89-221-215b

**Figure 6.** Carbon-fiber composite NMR samples used to measure the attenuation of the RF magnetic field. In (a) all carbon fibers are parallel to the cylinder axis; (b) all fibers are wound circumferentially around the cylinder axis; (c) 0° and 90-degree carbon-fiber plies are parallel to the coil axis; (d) 0° and 90-degree carbon-fiber plies are perpendicular to the coil axis.

because neither vacuum bagging nor mechanical pressure was applied during curing. Sample XPL contained 0°, 90° cross-ply oriented with the ply planes parallel to the coil axis, and sample XPR contained 0°, 90° cross-ply oriented perpendicular to the coil axis.

Hydrogen NMR measurements were conducted at 300 MHz in our Bruker MSL-300 spectrometer using a solenoidal coil of 10-mm inside diameter. The composite samples detuned the probe considerably from tuning on water only. Proper tuning was achieved for all samples by incorporating variable capacitors in both the phase and impedance sides of the probe circuit. The Q of

the probe, the duration of the pulsed RF magnetic field needed to achieve a 90-degree rotation of the hydrogen nuclei,  $\tau_{90}$ , and the integrated NMR signal of the water,  $S$ , were measured. The applied RF power was held constant at approximately 530 watts during these experiments. The signal,  $S$ , measures the attenuation of the NMR signal as it propagates out from the water, and  $1/\tau_{90}$  [see Equation (10)] measured the attenuation of the RF field as it propagates into the water. Since these attenuations should be equal, we expect the product  $S\tau_{90}$  to be a constant.

The RF magnetic field at the surface of these samples can be approximated by summing the RF fields of the probe coil and a coaxial image coil (in effect, a coil giving fields replicating the induced eddy currents) located inside the sample. The conductivity to use in the skin-depth calculations is the effective conductivity along the current paths defined by this image solenoid.

The current path in sample U (fiber axes unidirectional along the RF magnetic field direction) is everywhere perpendicular to the carbon-fiber axes; the effective conductivity in this case is  $\sigma_{\perp}$ . A small attenuation is therefore predicted, and the attenuation factor was measured to be 0.55, as shown in Table 7. Using Equation (9), the effective conductivity perpendicular to the fibers,  $\sigma_{\perp}$ , was found to be 25 S/m.

The current path in sample C (fibers circumferentially wound about the axis of the cylinder) is everywhere parallel to the carbon-fiber axes, and a large attenuation is predicted. The measured amplitude factor was 0.005, and Equation (9) yields a conductivity of 1,900, a factor of 18 smaller than the value of 49,000 predicted from Equation (6). This discrepancy could be the result of poor fiber consolidation or broken fibers, due to the difficulty in tightly wrapping the carbon-fiber prepreg around the 1-mm-diameter mandrel without breaking the fibers. A more likely explanation is that the connecting leads to the solenoidal probe coil produced components of the RF magnetic field that were in a direction to induce currents perpendicular to the fibers, and thereby experienced much less attenuation. Moreover, the fiber winding would have to be in nearly exact alignment with the RF coil for very high attenuations to be observed. RF leakage along the open, 1-mm hole may have also contributed to the small observed conductivity.

The current paths in sample XPL (containing  $0^{\circ}$ ,  $90^{\circ}$  cross-plyes oriented parallel to the cylinder axis) are both along the fiber axes and

across the plies. Since the conductivity across the plies,  $\sigma_{\perp i, i+1}$ , is about 1,000 times smaller than that along the fibers,  $\sigma_{\parallel}$ , the result is dominated by  $\sigma_{\perp i, i+1}$ , as follows from Equation (5). Thus, the predicted attenuation is small, and the amplitude factor was measured to be 0.32, corresponding to an effective conductivity of 120 S/m, or  $\sigma_{\perp i, i+1} = 170$  S/m, in good agreement with NMR imaging results presented below.

The current paths in sample XPR are effectively parallel to the fiber axes (in one ply for two sides of the eddy current loop, and in the adjacent ply for the other two sides of the loop), so a large attenuation is predicted. Table 7 shows the amplitude factor to be 0.05, which yields an effective conductivity of 840 S/m, much lower than the calculated value of 49,000 S/m. As was the case with sample C, this discrepancy was probably caused by stray RF magnetic fields arising from imperfections in the RF coil and to leakage along the 1-mm hole.

Table 7. Nonimaging NMR RF attenuation results for carbon-fiber composite samples.

Configuration <sup>(1)</sup>	Integrated NMR signal of water <sup>(2)</sup> S	Duration of 90° pulse, <sup>(3)</sup> $\tau_{90}$ ( $\mu$ s)	Probe Q	$S \tau_{90}$ ( $\mu$ s)	$\frac{S}{\sqrt{Q}}$	$\tau_{90} \sqrt{Q}$ ( $\mu$ s)
Water alone	1.00	1.30	165	1.30	0.078	16.7
(a) Fibers parallel to cylinder axis	0.55	2.3	55	1.27	0.074	17.0
(b) Fibers wound circumferentially	0.005	150	27	0.75	0.001	780
(c) Plies parallel to coil axis	0.32	3.85	23	1.23	0.067	18.5
(d) Plies perpendicular to coil axis	0.05	25	23	1.25	0.010	120

\* (1) See Figure 6.

(2) Relative to water alone

(3) Fixed if power level of approximately 530 watts

89-221-242a

**3.4.5 NMR Imaging Measurements** We find that the NMR imaging measurements of electrical conductivity are more accurate than the network analyzer and nonimaging measurements described above because NMR imaging is much less susceptible to errors caused by leakage of the RF magnetic field around or into the sample. This problem is avoided because the samples used for NMR imaging completely surround the detected phantoms, and spatial selectivity

obtained by use of imaging volume selection techniques and surface coils allow detection of only the region of interest.\*

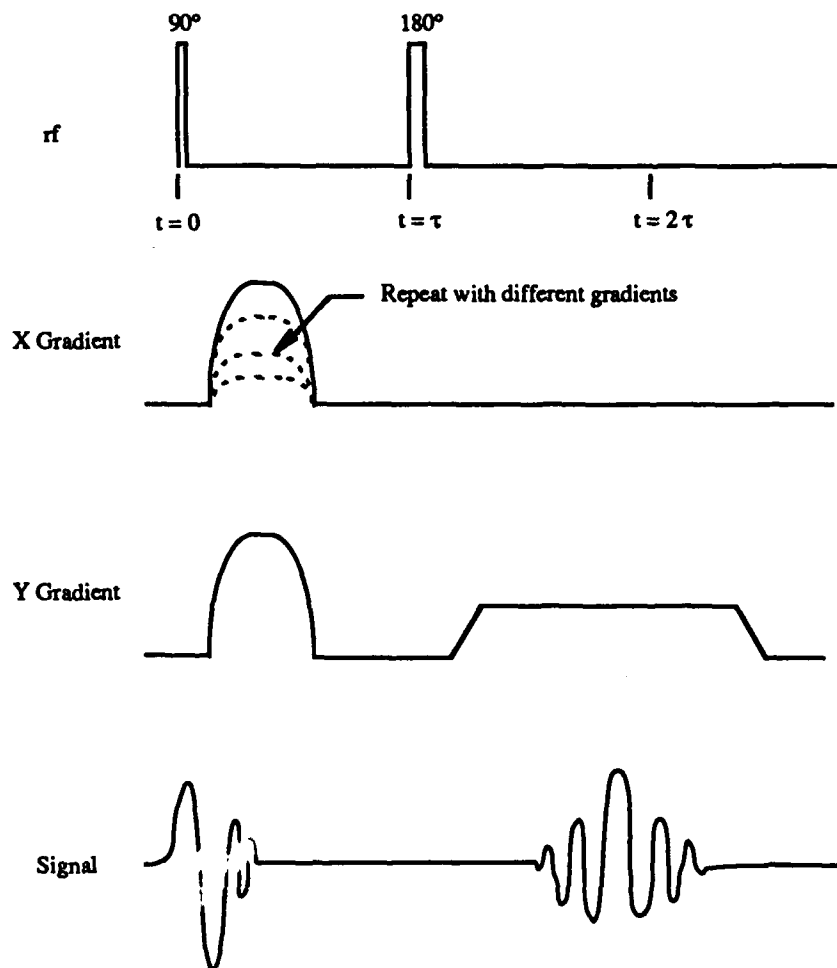
Hydrogen NMR imaging measurements were made at 85 MHz using a General Electric CSI 2-T magnetic resonance imaging spectrometer with a 310-mm bore. Shielded gradient coils produced gradients of greater than 2 mT/cm, with rise and fall times of less than 1 ms. A large-volume, bird-cage RF coil (Ref. 61) was used, which allowed imaging samples 100 mm in diameter. A surface coil was also used which precisely defined the entry point and polarization of the RF magnetic field. Two-dimensional images were obtained using the imaging pulse sequence shown in Figure 7, which is a variant of Fourier imaging (Ref. 62). An echo time  $\tau_e = 1$  ms and magnetic field gradients of 0.35 mT/cm were used to obtain all the results presented in this section.

Attenuation of the RF magnetic field was measured in 7- x 7-cm cross-ply ( $N=2$ ,  $\alpha_1=0^\circ$ ,  $\alpha_2=90^\circ$ ), unidirectional ( $N=1$ ,  $\alpha_1=0^\circ$ ), and chopped-carbon-fiber ( $\approx 6$ -mm length) panels containing 1- x 3- x 7-mm phantoms made of cut rubber bands placed at various depths from the surface and at various locations from the edges. A series of measurements were made on a cross-ply panel to determine the conductivity parallel to the plies,  $\sigma(90^\circ, \phi)$  (appropriate for imaging the center of a large panel), and in a direction perpendicular to the plies,  $\sigma(0^\circ, \phi)$  (appropriate for imaging the edge of a panel).

A surface coil with its axis parallel to the surface of the cross-ply panel and nearly touching the surface, as shown in Figure 5(b), was used to measure  $\sigma(90^\circ, \phi)$ . The static magnetic field was normal to the plies, and the RF magnetic field was parallel to the plies. NMR images were obtained of rubber-band phantoms mounted on the surface of cardboard as a reference, mounted on the surface of the cross-ply panel, and located 0.25, 0.5, 1.0 and 2.0 mm below the surface of the cross-ply panel. The reference image was obtained with a 25- $\mu$ s, 90-degree RF pulse using a transmitter power of 21 W. For all measurements, the RF pulse length and transmitter power were adjusted to produce the 90- and 180-degree pulses needed for the imaging experiment, with the transmitter power ranging from 21 to 94 W. An image of

---

\*NMR imaging is a useful technique for accurately measuring RF magnetic field strengths when the presence of pickup coils alter the value of the fields being measured.

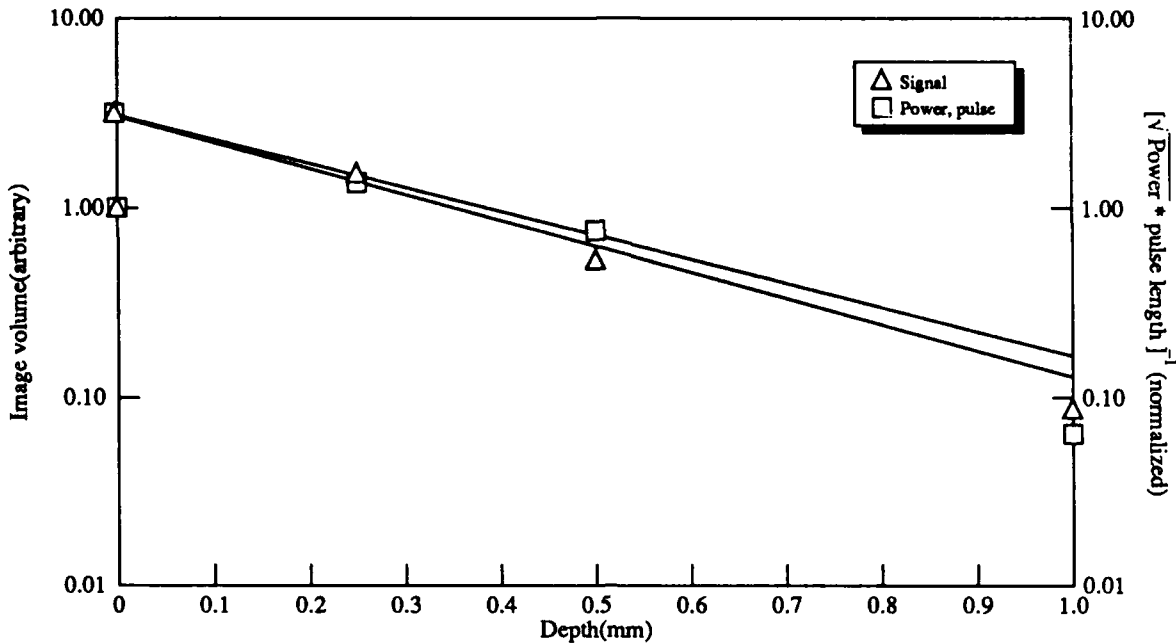


89-221-216

Figure 7. NMR imaging experiment pulse sequence and resulting NMR signal.

the sample at 2-mm depth could not be obtained because of the large RF attenuation at this depth.

The normalized image volume and the inverse of the normalized 90-degree pulse length multiplied by the square root of the transmitter power [see Equations (10)-(11)] are plotted in Figure 8 as a function of depth in the sample configurations listed above. Both sets of data at zero depth (i.e., a rubber-band phantom mounted on the surface of the panel) show that the amplitude of the RF magnetic field next to the surface of the panel is increased by a factor of three as a result of the induced surface currents. Opposite the attenuation effect of the eddy currents which decreases the strength of the RF magnetic field inside the sample, the eddy currents increase the RF magnetic field strength just outside the the ample between



89-221-217b

Figure 8. Measured attenuation of the RF magnetic field caused by a carbon-fiber cross-ply composite panel as the field propagated into the face of the sample perpendicular to the plies (along  $\theta = 180^\circ$ ). Data for both the reduction in image volume and the inverse pulse length multiplied by the square root of the transmitter power necessary to achieve a 90-degree RF pulse rotation are shown. The lines are the best fits to the data.

the surface of the sample and the coil. Use of the measured image volumes in Equation (8) yield  $\sigma(90^\circ, \phi) = 29,000$  S/m, and the pulse-length-and-power data yield  $\sigma(90^\circ, \phi) = 26,000$  S/m. These results give  $\sigma_{||}$  equal to 74,000 or 83,000 S/m, in reasonable agreement with the manufacturer's value of 70,000 S/m.

The bird cage coil was used to determine  $\sigma(0^\circ, \phi)$  in the cross-ply sample. The sample was 8 mm thick and had an oil phantom which extended from the center to one edge of the panel and was located between the two plies at the center of the panel. This panel was well consolidated, and no ply separation occurred except in the immediate vicinity of the phantom. The transmitter power was held constant at 2.25 kW, and a series of images were obtained as the pulse length was incrementally increased. The length of the 90-degree pulse in the absence of the carbon-fiber sample was 30  $\mu$ s. The static magnetic field was oriented perpendicular to the plies, and the RF magnetic field was parallel to the plies.

The field directions here are the same as in the experiments described above for measuring  $\sigma(90^\circ, \phi)$ . However, in those experiments, a surface coil was used at the location of a phantom beneath the surface, and the RF magnetic field propagated inward normal to the plies. Here, the phantom is far from the surface (4 mm). Therefore, the propagation inward and normal to the plies experiences very large attenuations, and the propagation that is observed instead comes in from the panel edge, parallel to the plies.

An RF pulse of a particular length  $\tau_{90}$  rotates by 90 degrees the  $^1\text{H}$  at the edge of the sample. The pulse rotation angle,  $\theta$ , is related to the pulse length,  $\tau_\theta$ , and power,  $P$ , as follows [see Equations (10)-(11)]:

$$\theta \propto \tau_\theta \sqrt{P} . \quad (12)$$

The RF power decreases exponentially with increasing depth into the sample according to Equation (9), as does the pulse rotation angle. From Equations (9) and (12), we see that when  $\tau_\theta$  is increased, the position of the 90-degree rotation moves deeper into the sample. At  $2\tau_{90}$  RF pulse lengths, the  $^1\text{H}$  nuclei at the edge of the sample experience a 180-degree rotation, and a null appears in the image at this point (i.e., these  $^1\text{H}$  nuclei do not contribute to the observed transverse magnetization). As  $\tau_\theta$  is increased from  $\tau_\theta = 2\tau_{90}$ , the null moves deeper into sample. The position of the null thus provides an accurate position for the volume element at which a 180-degree rotation is occurring, and this position as a function of pulse length,  $\tau$ , provides information from which, by use of Equation (9), we can quantify  $\sigma(0^\circ, \phi)$ . The reciprocal of the pulse lengths are plotted as a function of the null positions in Figure 9, which yields  $\sigma(0^\circ, \phi) = \sigma_{\perp 1,1+1} = 130 \text{ S/m}$ , in agreement with the results for sample XPL.

RF attenuations smaller than those predicted were observed in samples containing large delaminations caused by the irregular shapes of the phantom and/or in samples that had poor consolidation during curing. The effect of delaminations on RF propagation deserves further mention. The region between two conducting aluminum plates in close proximity, but separated by an electrical insulator, can be imaged if the RF magnetic field is applied parallel to the plane of the plates (Ref. 63). For this polarization, the induced eddy currents must cross the electrical insulator, so negligible RF attenuation occurs.

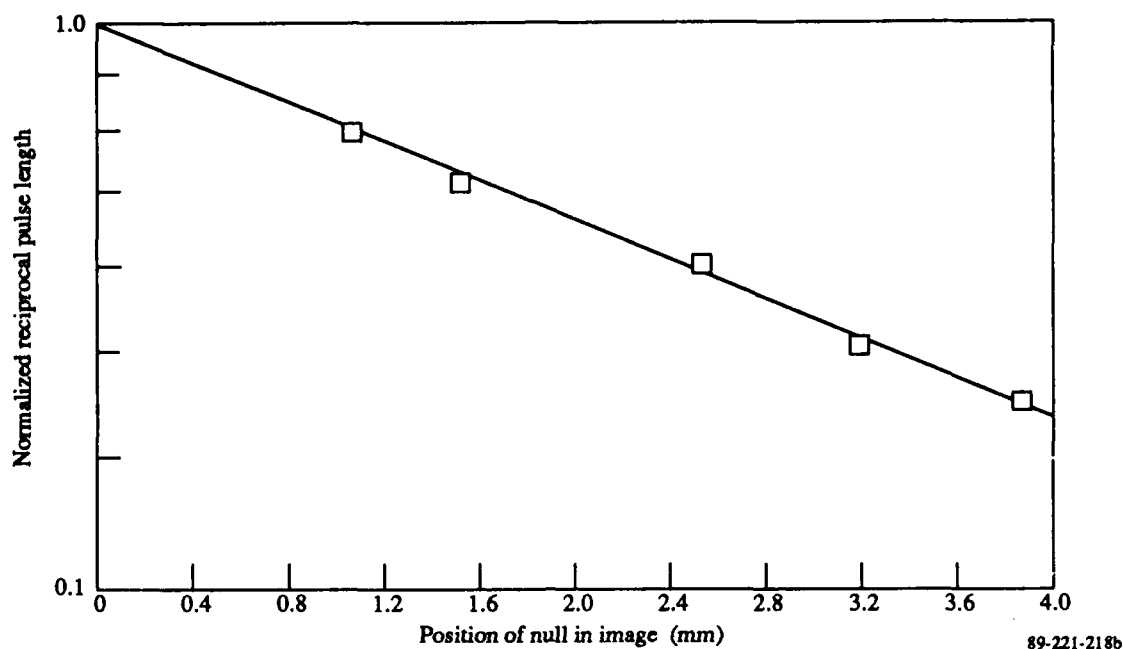


Figure 9. Measured attenuation of the RF magnetic field caused by a carbon-fiber cross-ply composite panel as the field propagated into the edge of the sample parallel to the plies (along  $\theta = 90^\circ$ ). The line is the best fit to the data.

Another case in which small attenuations of the RF magnetic field were observed occurred when the carbon fibers were cut. In one case, we drilled a hole through the plies, inserted a phantom, and replugged the hole with a close-fitting carbon-fiber composite piece. The NMR image we observed had an amplitude at least 30 times larger than that from an identical phantom incorporated behind continuous fibers.

A chopped-carbon-fiber panel having randomly oriented (or perhaps oriented slightly parallel to the plane of the panel), 6-mm-long fibers was imaged, and was found to have an effective (isotropic) conductivity similar to, but somewhat less than,  $\sigma(90^\circ, \phi)$  of the cross-ply composite. Because fiber length, orientation, consolidation, and volume fraction all strongly affect the conductivity, the study of chopped, carbon-fiber samples was not continued. More importantly, the size of the attenuation observed was sufficient to group the assessment of NMR and NMR imaging of chopped-fiber materials with the assessment of cross-ply materials where the RF is propagating in through the face of the panel, i.e.,  $\sigma(90^\circ, \phi)$ .

**3.4.6 Discussion** Table 8 summarizes the values of the components of the electrical conductivity of AS-4/3501-6 carbon fiber epoxy composites



**Table 8. Summary of predicted and measured values of the components of the electrical conductivity of AS-4/3501-6 carbon-fiber epoxy composites.**

Component	Predicted (S/m)	Measured (S/m)	Measurement Technique
$\sigma_{  }$	70,000 <sup>a</sup>	66,000 $\pm$ 34,000 74,000 to 83,000	Network analyzer NMR imaging
$\sigma_{\perp}$	b	0.3 to 11 <sup>c</sup> 25	Network analyzer Nonimaging NMR
$\sigma_{\perp, i+1}$ for 0°, 90° cross-ply	b	120 130	Nonimaging NMR NMR Imaging

<sup>a</sup> Using manufacturer's value, Ref. 12

<sup>b</sup> Not predictable

<sup>c</sup> Measured values are lower bounds

determined by use of the various techniques, but excluding the values of conductivities determined from experiments in which stray fields were suspected to have seriously affected the results. In all cases, the measured conductivities were large enough to satisfy the conditions for the carbon-fiber composite to be classified as a good conductor [see Equation (7)]. These results allow a more definitive discussion of NMR and NMR imaging of carbon-fiber composite materials that also satisfy the condition that their size is large compared to the skin depth  $\delta$ , [Equation (8)].

To assess the effects of the carbon fibers on NMR and NMR imaging of OMC materials, the simplest way to begin is to consider the RF power requirements for NMR experiments of carbon-fiber composites. Equations (7)-(11) are combined to obtain the required RF power per unit area ( $W/m^2$ ) entering the surface of a carbon-fiber composite sample to produce a rotation  $\theta(d)$  of the nuclei at a depth,  $d$ , using an RF pulse of duration,  $\tau$ . The result is

$$P(0) = \left[ \frac{\theta(d)}{180 \gamma \tau \mu_0} \right]^2 (\pi \nu \mu_0 / \sigma)^{1/2} \exp[2d (\pi \nu \mu_0 \sigma)^{1/2}] . \quad (12)$$

The appropriate value of conductivity to use in Equation (12) is discussed following Equation (9). Equation (12) has the advantage that it is not dependent upon the geometry of the sample or RF coil. It simply states the RF power dissipated per unit area in the sample due to ohmic losses, given

the desired RF magnetic field at some location,  $d$ , in the sample. This equation shows that the required transmitter power can be reduced by reducing the area of the sample being imaged.

Equation (12) can be used to compute representative required RF powers per unit area provided some reasonable assumptions are made. First, we assume that hydrogen nuclei are being imaged so that  $\gamma = 42.57 \text{ MHz/T}$ . Also, since solid-state experiments require rapid rotation of the nuclei, we assume that an RF pulse of duration  $\tau = 5 \mu\text{s}$  will be required to produce a rotation  $\theta(d) = 90^\circ$ . Using these values in Equation (12), the required RF power per unit area can be calculated for different operating frequencies,  $\nu$ , depths,  $d$ , and conductivities,  $\sigma$ , corresponding to different sample orientations relative to the RF magnetic field. These results are shown in Figure 10 for propagation into the cross-ply sample, along the direction  $\theta = 180^\circ$ , where  $\sigma = 25,000 \text{ S/m}$ .

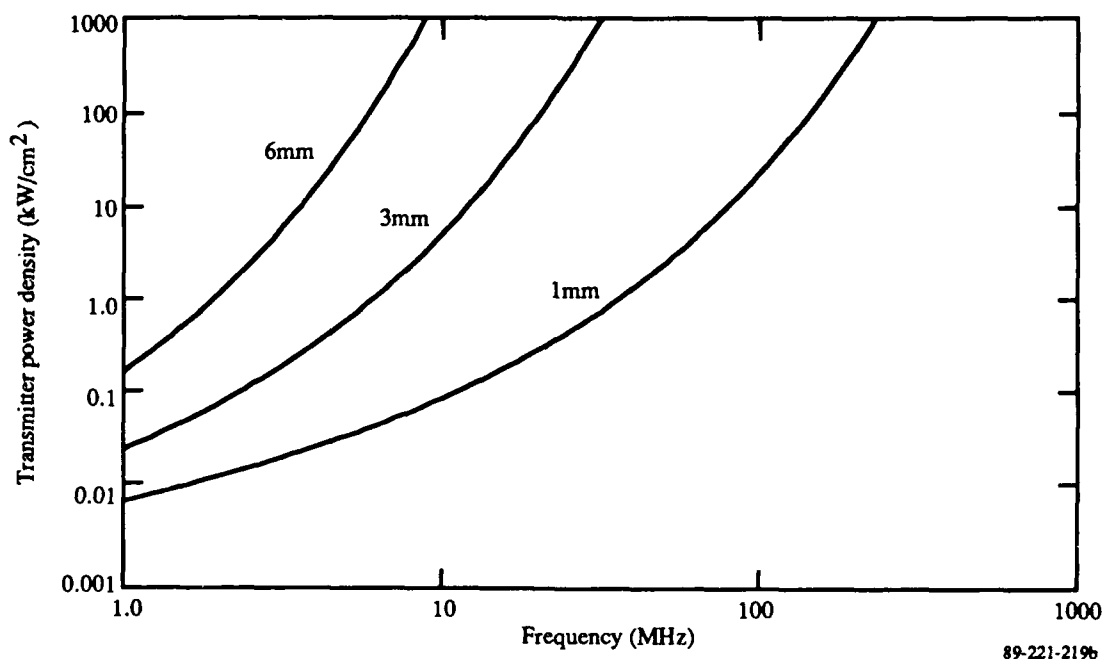


Figure 10. The transmitter power density required to generate a 5- $\mu\text{s}$ , 90-degree rotation of hydrogen nuclei as a function of frequency in a cross-ply carbon-fiber composite sample where the RF propagation is perpendicular to the plies (along  $\theta=180^\circ$ ). Curves are plotted for hydrogen nuclei at 1-, 3- and 6-mm depths into the cross-ply sample.

If we assume that  $5 \text{ kW/cm}^2$  is the maximum transmitter power density available (larger transmitters might be feasible, but the power dissipation becomes so large that sample heating becomes a significant issue), and

10 MHz is a minimum usable frequency (we discuss going to lower frequencies in Section 4.0), Figure 10 shows that 3-mm depths are already inaccessible. Even when mobile hydrogen (i.e., for an invasive fluid or solvent) is observed, in which case  $\tau_{90}$  can be increased by an order of magnitude, 6-mm depths are still inaccessible.

Transmitter power is only one potential problem caused by the conductive nature of the carbon-fibers. Power dissipation, variation in the RF pulse rotation angles, and especially sensitivity as a function of depth into the material become significant issues. The relative sensitivity of constant densities of hydrogen nuclei as a function of frequency and depth can be roughly approximated in these materials. If  $T_1$  dependencies and variations in probe constructions we ignored (we address these dependencies in the assessment made in Section 4.0), the signal-to-noise (S/N) depends approximately on  $\nu^{3/2}$  for a non-lossy material.\* Since the S/N is linearly dependent on the induced voltage caused by the nuclear magnetic moments, which experience attenuation governed by Equation (8), we have

$$S/N(\nu, d) \propto \nu^{3/2} \exp\{-d(\pi\mu \nu\sigma)^{1/2}\} . \quad (13)$$

This function is plotted in Figure 11 for a non-lossy material ( $d=0$ ), for depths of 1, 3, and 6 mm. Going to 10 MHz at 3-mm depth, the S/N is reduced by a factor of 300 from a non-lossy material at 85 MHz. To obtain the same S/N at 10 MHz with a cross-ply composite material as at 85 MHz with a non-lossy material (i.e., nominal NMR), the experiment might take 100,000 times longer. In Section 4.0, we show that  $T_1$  considerations do not improve this

---

\* W. G. Clark, Pulsed Nuclear Resonance Apparatus, Rev. Sci. Instrum. 35(3), 316 (1964), Eq. 12(a). In D. I. Hoult, The NMR Receiver: A Description and Analysis of Design, Prog. NMR Spec. 12, 41 (1978),  $\alpha$  in Clark's Eq. 12(a) is shown to be proportional to  $\nu^2$ , so that  $S/N \propto \nu^{3/2}$  for non-lossy materials. Although this is an approximation, the  $\nu^{3/2}$  dependence best follows empirical data [see, for example, Bruker Almanac 1989 (Bruker Instrum., Inc. 1989, p. 92)]. The exact power of  $\nu$ , however, does not affect the conclusions about RF attenuation as a function of frequency to any great extent. Much more important is the value of  $\sigma$  for the system being studied.

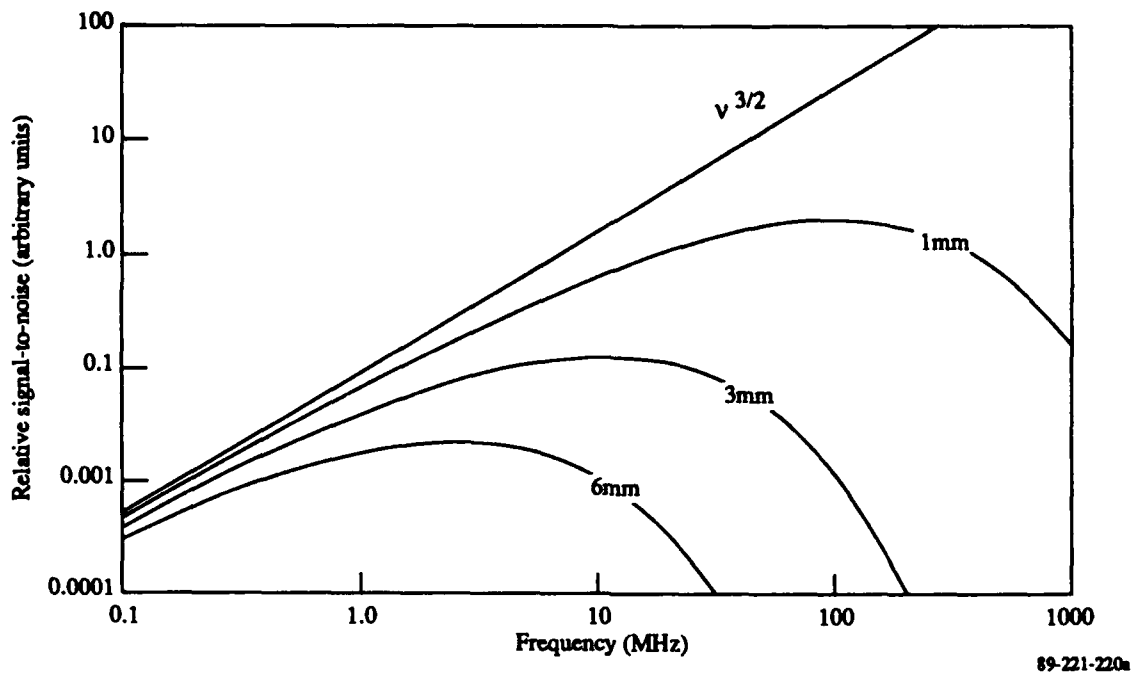


Figure 11. The relative signal-to-noise for NMR and NMR imaging experiments as a function of frequency in a cross-ply carbon-fiber composite sample where the rf propagation is perpendicular to the plies (along  $\theta = 90^\circ$ ). Curves are plotted for hydrogen nuclei at 1-, 3- and 6-mm depths into the cross-ply sample. The straight line is the S/N dependence expected from a non-lossy sample.

situation much. Whereas in NMR imaging of non-lossy materials, we would want as high a static magnetic field strength (and thus a high frequency) as possible for S/N reasons, this possibility is excluded because of the conducting nature of the sample. The decreasing S/N with increasing frequency behavior, displayed in Figure 11, is observed in other related areas. At very high frequencies, such as the case for electron spin resonance, lower S/N values are observed when going to higher static magnetic field strengths in studies of lossy materials (Ref. 64). Thus, although Equation (13) is an approximate relationship, going to lower static magnetic field strengths and thus decreasing the S/N substantially in comparison to nominal NMR, is necessary for NMR to have any possibility of imaging OMC.

These considerations along with the transmitter power requirements shown in Figure 10 indicate that NMR and NMR imaging of features at depths  $\geq 3$  mm in carbon-fiber cross-ply (and similarly, chopped fiber) composites at frequencies  $\geq 10$  MHz (0.235 T) is not feasible when the RF must propagate perpendicular to the plies. Even if technical advances are made in experimental design of probes, only a millimeter or two improvement seems pos-

sible. Also, for flaws such as delaminations and broken fibers, where the eddy current pathways are broken, the RF must first reach the area of the flaw. Unless the delaminations or broken fibers propagate from close to the surface, RF attenuation will prevent detection as it does with other features. Nominal NMR and NMR imaging do not therefore appear to be viable NDE techniques for the inspection of large-scale carbon-fiber composite pieces such as wing-skins. Assessment and possible designs of low-field NMR spectrometers are discussed in Section 4.0.

Equation (12) can be evaluated for propagation parallel to the plies ( $\theta=90^\circ$ ), where  $\sigma = 130$  S/m instead of 25,000 S/m. Figures 12 and 13 show the transmitter power density and relative S/N, respectively, for this experimental arrangement as a function of frequency and depth. Note that 1-cm depths could probably be imaged even at 35 MHz, and that the S/N is much improved as compared to propagation perpendicular to the plies (see Figure 11). Considering that propagation parallel to the plies must come from an edge, being able to study only 1 cm is very limiting. Still, NMR and NMR imaging might be viable for studying joints, drop-off regions, and bulk properties close to edges of carbon-fiber composite structures.

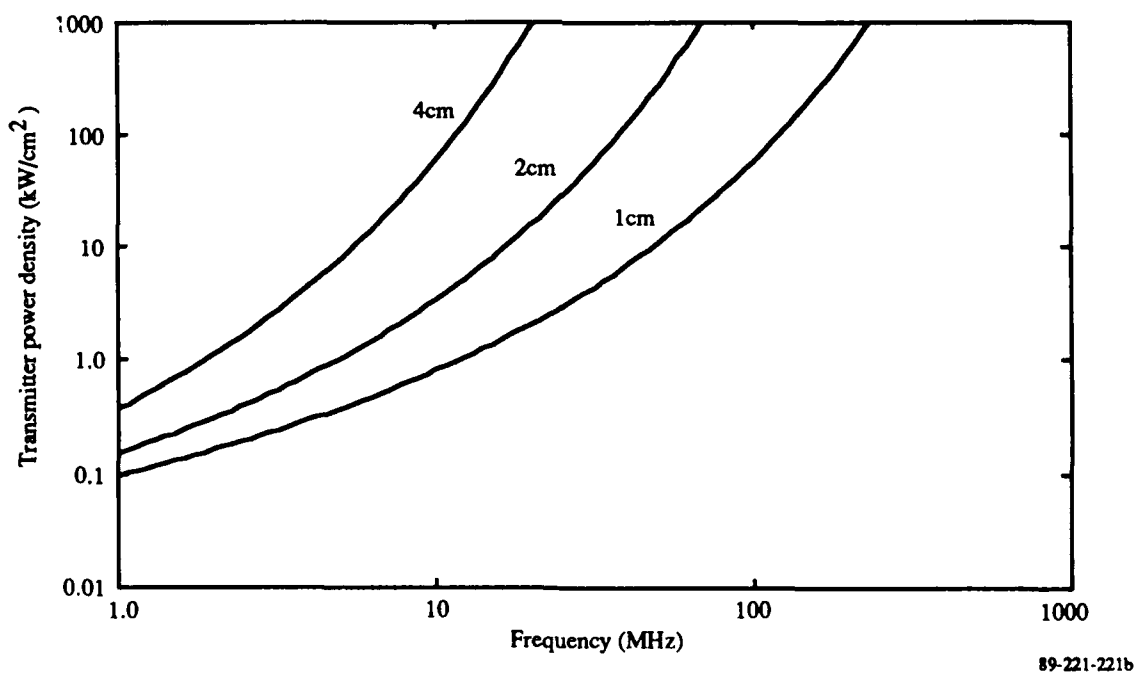


Figure 12. The transmitter power density required to generate a 5- $\mu$ s, 90-degree rotation of hydrogen nuclei as a function of frequency in a cross-ply carbon-fiber composite sample where the RF propagation is parallel to the plies (propagation along  $\theta = 90^\circ$  and E field along  $\theta = 0^\circ$ ). Curves are plotted for hydrogen nuclei at 1-, 2 - and 4-cm depths in from the edge of the cross-ply sample.

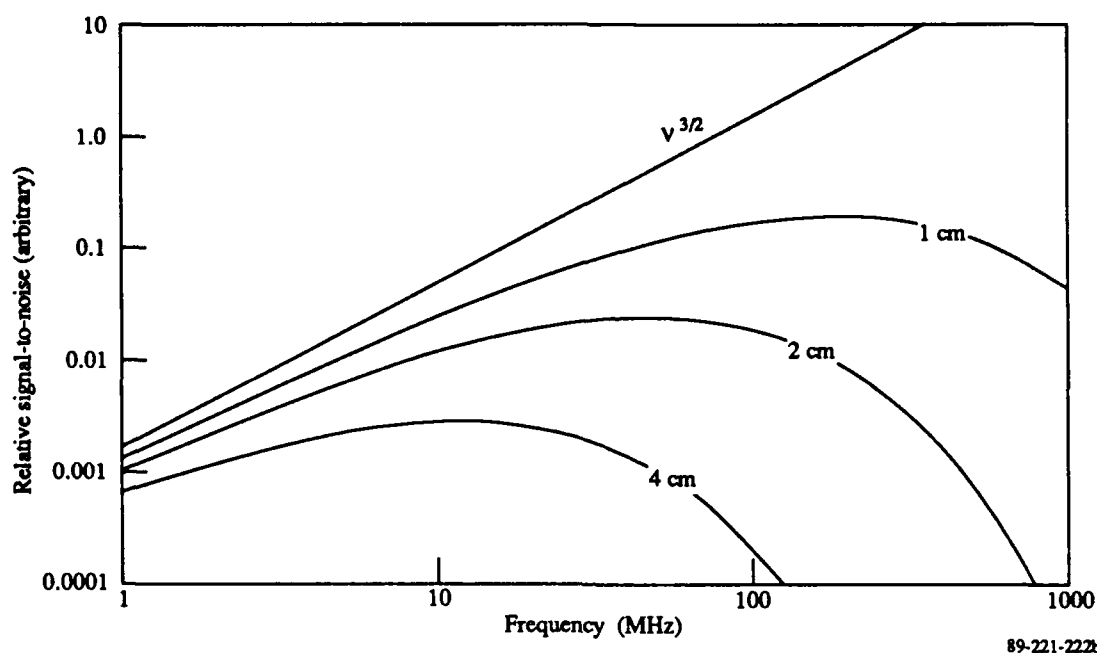


Figure 13. The relative signal-to-noise as a function of frequency in a cross-ply carbon-fiber composite sample where the RF propagation is parallel to the plies (propagation along  $\theta = 90^\circ$  and E field along  $\theta = 0^\circ$ ). Curves are plotted for hydrogen nuclei at 1-cm, 2-cm, and 4-cm depths in from the edge of the cross-ply sample. The straight line is the S/N dependence expected from a nonlossy sample.

### 3.5 $^{129}\text{Xe}$ and Liquid/Vapor Sorption Experiments

NMR of  $^{129}\text{Xe}$  has been observed in clathrates (Ref. 65) and zeolites (Ref. 66), and recently in low-density polyethylene (Refs. 67,68). These studies indicate that if  $^{129}\text{Xe}$  would sorb into defect areas of organic composites, we could use conventional magnetic resonance imaging (MRI) techniques to study the defects nondestructively.

Four samples were prepared for the  $^{129}\text{Xe}$  study with our MSL-300 spectrometer. For all the samples, 0.015 MPa of xenon gas containing 26.4%  $^{129}\text{Xe}$  isotope (natural abundance) was introduced into our vacuum system, and 0.036 MPa of  $\text{O}_2$  was added. Cooling the 10-mm o.d. sample tube to 77 K with a vacuum system volume of 235  $\text{cm}^3$ , sealing to a sample tube volume of about 6.5  $\text{cm}^3$ , and reheating to room temperature produced about 1.1 MPa of 50%  $^{129}\text{Xe}$  (13%  $^{129}\text{Xe}$ ) and 50%  $\text{O}_2$  gas. The four samples were (1) pure gas, (2) neat solid PEEK, (3) crushed neat epoxy resin (Shell Epon 9405/9470), and (4) neat solid epoxy resin with known voids. The fourth sample of Shell Epon 9405 resin/9470 curing agent was cured at 170°C and ambient pressure for 4 h, and optical and scanning electron microscopy showed the presence of 0.5-

to 1- $\mu$ m-dia. voids filling about 2% of the sample volume.

The pure gas sample yielded the results we anticipated. We observed a single resonance line having a linewidth,  $\Delta\nu$ , of 20 Hz (full width at half-height), and a  $T_1$  of 0.35 s (thus, an experiment could be repeated every 2 s). The  $O_2$  acted as a paramagnetic relaxation agent, lowering  $T_1$  of the  $^{129}\text{Xe}$  from 55 h (Ref. 69) to 0.35 s. A reasonable signal-to-noise (S/N) ratio was obtained using our liquids 10-mm probe (i.e., the same RF system as used in conventional MRI equipment) in one experiment, i.e., every 2 s.

Unfortunately, the other three samples, each containing polymeric resin, did not produce any new observable resonances. Figure 14 shows a typical  $^{129}\text{Xe}$  NMR spectrum of the crushed epoxy sample. Any interpretation of the broad resonance down-field from the gas peak (at 0 ppm) is ambiguous at this time because the probe has a smaller, but nonnegligible background signal in the same region. A total of 14 h was needed to obtain this spectrum.

The inability to observe  $^{129}\text{Xe}$  resonances in the polymeric samples in reasonable experimental times is most likely due to a combination of unfavorable factors. The following relationships are appropriate in this context:

$$S/N \propto \rho(T_1\Delta\nu)^{-1/2} \quad (14)$$

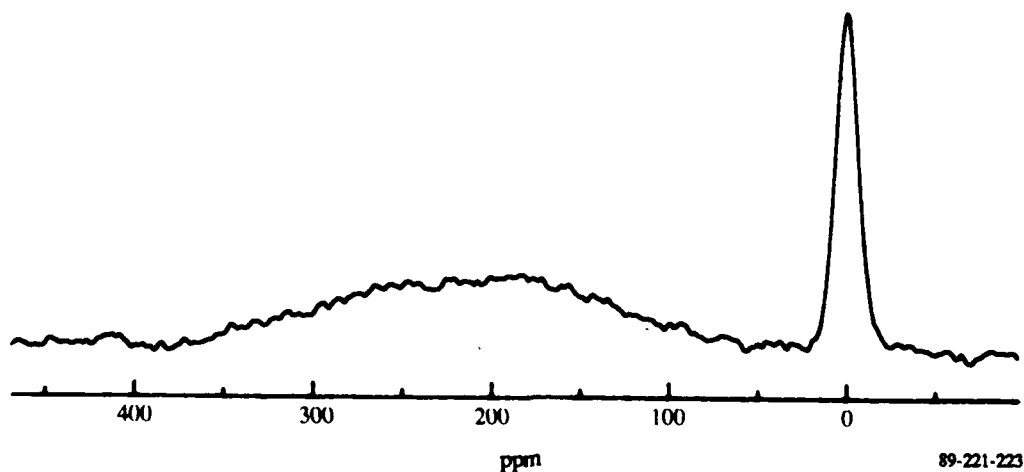


Figure 14.  $^{129}\text{Xe}$  NMR spectrum of sample (3).

and

$$TE \propto (S/N)^2 \quad + \quad TE \propto \rho^2 / (T_1 \Delta\nu) \quad (15)$$

where TE is the total experimental time to produce a particular S/N ratio,  $\rho$  is the  $^{129}\text{Xe}$  density, and  $\Delta\nu$  is the resonance linewidth. The lower  $^{129}\text{Xe}$  density,  $\rho$ , in the samples (Refs. 67-70) compared to the gas, greatly increases the experiment time needed to produce an acceptable S/N ratio. For the epoxy resin containing 2% voids, we might expect to observe  $^{129}\text{Xe}$  in 1 h ( $TE = 2s/(0.02)^2 = 5,000$  s), assuming that the resonance linewidth  $\Delta\nu = 20$  Hz. In unfavorable conditions,  $\Delta\nu$  might become as large as 8 kHz (as is apparently the case in epoxies), which would increase the experiment time by a factor of 400. In low-density polyethylene and in zeolites,  $^{129}\text{Xe}$  linewidths are small, but in PVC the linewidth is large (Ref. 70). Apparently, epoxies and PEEK must have large  $^{129}\text{Xe}$  linewidths, negating the utility of  $^{129}\text{Xe}$  NMR for NDE of organic composite materials; therefore, we have determined that  $^{129}\text{Xe}$  NMR is not a useful invasive fluid for NDE of organic composites.

$^{13}\text{CO}_2$  is another invasive fluid that might be useful for the NDE of OMC. However, the large cross-sectional area of  $\text{CO}_2$  and experience infers that equilibration times of this fluid into polymeric systems would be long ( $\sim 2$  days; Ref. 71). We have not, therefore, pursued this approach.

### 3.6 $^{13}\text{C}$ NMR Line-Narrowing and Imaging Experiments\*

Imaging with proton NMR is a difficult approach for solids (Refs. 27,45) because of the severe homonuclear dipole-dipole broadening effects (Refs. 47-49; see Section 3.7), so rare-spin techniques using  $^{13}\text{C}$  have been developed for solids (Refs. 3,4).  $^{13}\text{C}$  linewidths are dominated by heteronuclear dipole-dipole interactions in solid materials, but line narrowing can be achieved by applying a strong,  $^1\text{H}$ -decoupling RF pulse which is much less demanding than the multiple-pulse sequences needed to reduce homonuclear dipole-dipole broadening interactions (Refs. 48,49,72).

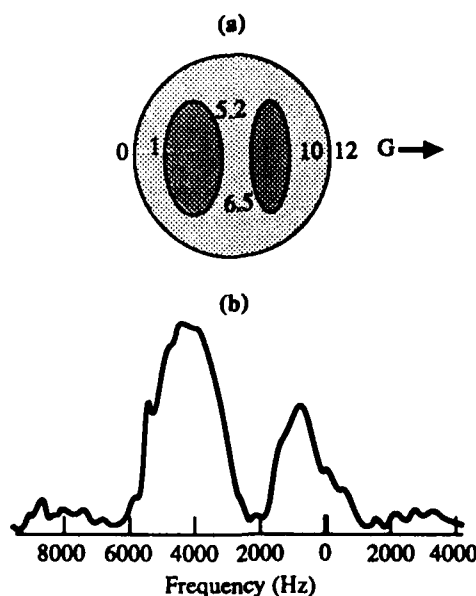
---

\* Much of this section of work is published as Ref. 2.



We have obtained  $^{13}\text{C}$  NMR images of aerospace polymers, and have demonstrated that both chemical shift and relaxation times can be used as contrast mechanisms in materials with large proton linewidths, e.g., having  $^1\text{H } T_2 < 20 \mu\text{s}$ . We have also obtained  $^{13}\text{C}$  chemical-shift images of small organic-matrix/carbon-fiber composites. These experiments demonstrate the feasibility of performing rare-spin NMR imaging of aerospace materials, and point to future experiments that will combine contrasting mechanisms to make NMR imaging truly useful for solid-state studies. These experiments also enable us to estimate total experimental times necessary to achieve a desired spatial resolution, and to compare relative advantages and disadvantages of  $^{13}\text{C}$  imaging to  $^1\text{H}$  imaging of solid materials.

The  $^{13}\text{C}$  NMR images were obtained with the CSU spectrometer consisting of a 2.3-T superconducting magnet, a  $^{13}\text{C}$ - $^1\text{H}$  double-resonance probe, one set of z-gradient coils (parallel to the static magnetic field direction - the coils are wound on the inside of the probe casing), the gradient power supply, RF electronics, and a computer (Ref. 3). The magnetic field gradient, G, was calibrated by use of a Teflon phantom, where holes of known sizes were filled with adamantane as shown in Figure 15(a). The  $^{13}\text{C}$  NMR image is shown in Figure 15(b), from which  $\gamma G = 8.0 \pm 0.5 \text{ kHz/cm}$  is derived.



89-221-224a

Figure 15. Calibration of the magnetic field gradient G: (a) The Teflon phantom containing two holes filled with adamantane, (b) the  $^{13}\text{C}$  image obtained from the phantom. The numbers show the extreme position along G in millimeters of each feature of the phantom.

The sequences used for  $^{13}\text{C}$  NMR imaging in this study are shown in Figures 16 and 17, and are referred to here as Exps. 1 and 2, respectively. All imaging experiments were performed without sample spinning. Data at 7.0 T were obtained on the Bruker MSL-300 spectrometer at MDRL.

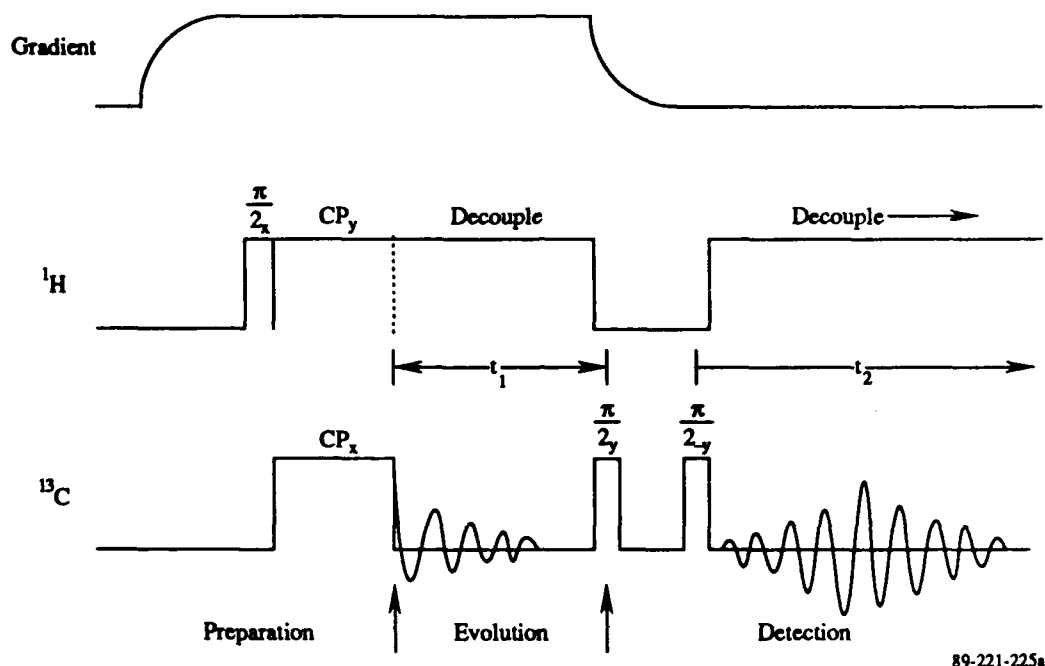


Figure 16. Schematic of the pulse sequence used to obtain  $^{13}\text{C}$  NMR chemical-shift images.

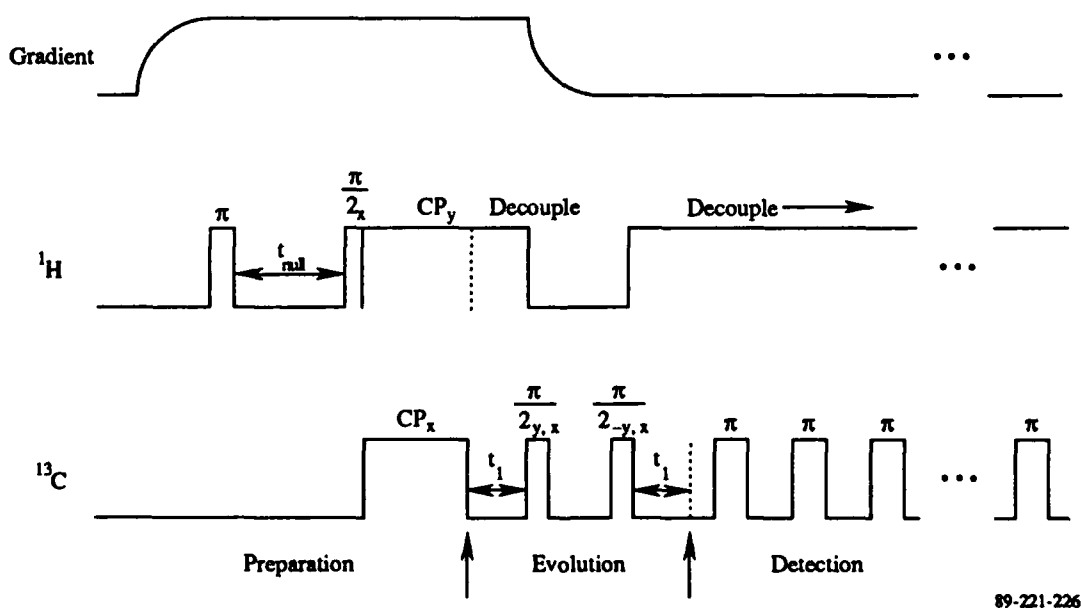
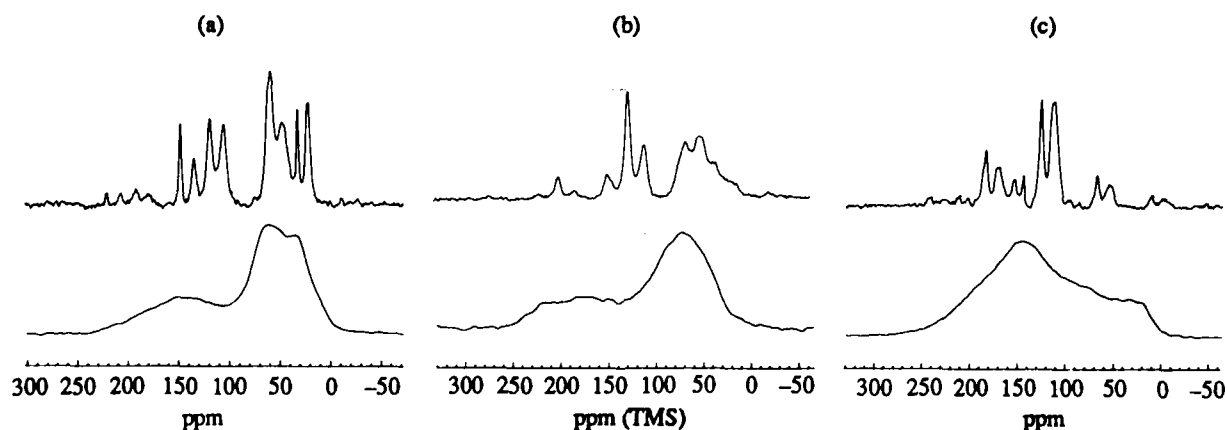


Figure 17. Schematic diagram of the pulse sequence used to obtain  $^{13}\text{C}$  NMR images with  $^1\text{H}$  spin-lattice relaxation as the contrast mechanism.

Samples used in this study are poly(aryl-ether-ether ketone), PEEK; the epoxy resin diglycidal-ether of bisphenol-A cured with 2,2'-diaminodiethylamine, DER/DETA; and their carbon-fiber laminate analogs APC-II obtained from ICI Americas (Wilmington, DE) and AS-4/3501-6 epoxy from Hercules Inc. (Magna, Utah). We also looked at the 3501-6 neat epoxy resin. Magic-angle spinning (MAS) and nonspinning cross-polarization (CP)  $^{13}\text{C}$  spectra obtained at 7.0 T on the two neat resins are shown in Figure 18. Important features of these spectra are the following:

1. The aromatic carbons display a large chemical-shift anisotropy of more than 200 ppm, whereas the aliphatic carbons have a chemical-shift anisotropy of about 20 ppm (as observed in many organic compounds, Ref. 73). A large chemical-shift anisotropy will reduce the intensity observed in a chemical-shift image, so the aromatic carbons should have a lower observable intensity when compared to the same number of aliphatic carbons.
2. The approximate experimental time to obtain a S/N ratio of 5 for various contact times is detailed in Table 9. The aromatic intensity can be made more intense with respect to the aliphatic carbons by use of a long contact time.



89-221-227a

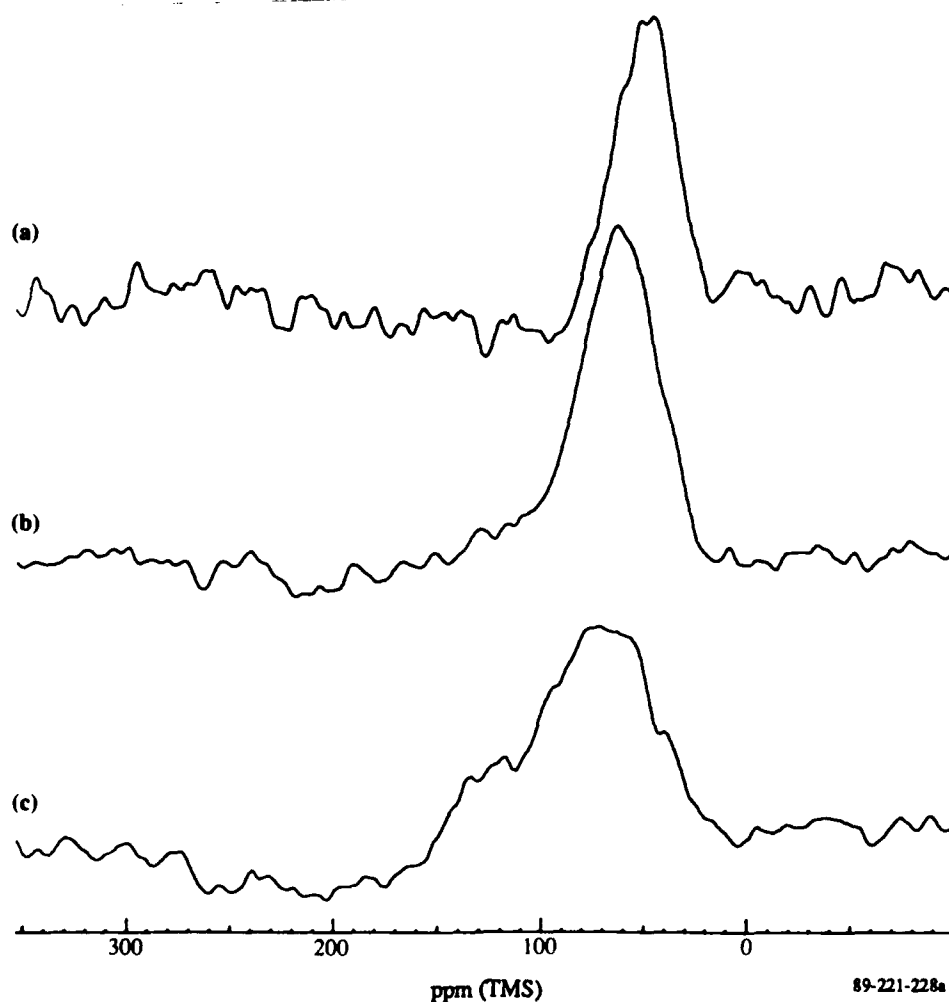
Figure 18.  $^{13}\text{C}$  CP/MAS spectra taken at 7.0 T of (a) DER/DETA epoxy resin spinning at 5.5 kHz (top) and nonspinning (bottom), (b) 3501-6 epoxy resin spinning at 5.5 kHz (top) and nonspinning (bottom), and (c) PEEK resin spinning at 4.3 kHz (top) and nonspinning (bottom).

**Table 9. Estimates of experimental times needed to obtain S/N = 5 on neat resins as a function of contact time.\***

Resin	Contact time (ms)	Experimental time (min)
DER/DETA	0.5	0.5
	1.0	4.2
	3.0	5.0
3501-6	0.5	4.0
	1.0	9.0
	3.0	10.3
PEEK XK300	0.5	22
	1.0	17
	3.0	9.5

\* Exponential line-broadening of 300 Hz applied to spectra obtained at 300 MHz.

89-221-244a



89-221-228a

**Figure 19.**  $^{13}\text{C}$  CP/MAS spectra with a selective  $3\pi/2$  pulse applied on the aliphatic chemical -shift region of (a) DER/DETA epoxy resin, (b) 3501-6 epoxy resin and (c) PEEK resin.

Figure 19 shows the static  $^{13}\text{C}$  spectra of all three samples where a selective RF read pulse, centered on the up-field portion of the chemical-shift range, was applied. The selective pulse attenuates the aromatic magnetization while preserving most of the aliphatic magnetization. Thus, using a selective pulse during the preparation portion of an imaging experiment, we should be able to contrast aliphatic (bright or intense) portions of the sample from aromatic (dark or weak) portions. For this experiment, a short contact time would be used, intensifying the aliphatic carbons with respect to the aromatic carbons.

An important parameter for imaging  $^{13}\text{C}$  in solids is  $T_2^\dagger$ , the relaxation time of the carbons under strong  $^1\text{H}$  decoupling and chemical-shift refocusing. This parameter depends primarily on the ability of the  $^1\text{H}$  decoupling to remove  $^{13}\text{C}$ - $^1\text{H}$  dipolar interactions, and directly affects the spatial resolution,  $\Delta x$ , obtainable in an image. The relationship between  $\Delta x$  (in cm) and the gradient size  $\gamma G$  (the maximum field gradient strength in  $\text{Hz}\cdot\text{cm}^{-1}$ ) is given by [see Equation (3) of Section 2.3 where  $1/(\pi T_2^\dagger) = \Delta\nu$ ]

$$\Delta x = [ \pi T_2^\dagger \gamma G ]^{-1} . \quad (16)$$

Moreover,  $T_2^\dagger$  affects the experimental signal-to-noise ratio,  $S/N$ , as (Ref. 74)

$$S/N \propto N_0 \gamma [T_2^\dagger]^{1/2} . \quad (17)$$

where  $N_0$  is the concentration of nuclei and  $\gamma$  is their magnetogyric ratio.

We have measured  $T_2^\dagger$  of PEEK and epoxy resin at MDRL in three similar ways. (As discussed below, the measurements at CSU were dominated by  $S/N$  considerations and truncation artifacts.) In the first method, we used Exp. 1 with zero applied gradient and determined  $T_2^\dagger$  from the diagonal half-linewidth at half-height,  $\nu_{1/2}$  ( $=\Delta\nu/2$ ), in the resulting two-dimensional Fourier transform by use of the relationship,  $\nu_{1/2} = 1/(2\pi T_2^\dagger)$ . In this measurement, only an upper bound of 25 Hz for both PEEK and epoxy could be determined for  $\nu_{1/2}$  because of the limited number of points used in the Fourier transform, as explained below.

An intrinsic Lorentzian line shape,  $S(\nu)$ , having  $T_2 = 1/(2\pi\nu_{1/2})$ , truncation in the time domain at time  $T = N \cdot DW$ , where  $N$  equals the number of

digital points in the detection period,  $t_2$  (see Figure 16) and DW is the dwell time, produces, after Fourier transformation, a modified line shape (Ref. 75):

$$S'(\nu) = \int_0^T \exp(-t/T_2) \exp(-i2\pi\nu t) dt \quad (18)$$

The linewidth  $\nu'_{1/2}$  of this modified line shape,  $S'(\nu)$ , can be determined from the root of

$$[\nu'_{1/2}]^2 - cZ \cos(2\pi\nu'_{1/2}T) = \frac{2c-1}{(2\pi T_2)^2} + cZ, \quad (19)$$

where  $Z = \exp(-T/T_2) / \{\pi T_2 [1 - \exp(-T/T_2)]\}^2$ , and  $c=1$  for a power spectrum and  $c=2$  for a magnitude spectrum. When  $T \gg T_2$ ,  $\nu'_{1/2} = \sqrt{2c-1} \nu_{1/2}$ , and when  $T < T_2$ ,  $\nu'_{1/2}$  becomes the half-width at half-height of the Fourier transform of the truncation function,  $S^t(\nu) = \int_0^T \exp(-i2\pi\nu t) dt$ ; i.e.,

$$\nu_{1/2}^t = \sqrt{2c} \sin(\pi\nu_{1/2}^t T) / (\pi T), \quad (20)$$

yielding  $\nu_{1/2}^t = 0.443/T$  for  $c = 1$  and  $\nu_{1/2}^t = 0.603/T$  for  $c = 2$ .

The first method was employed with a sweep width of 35,714 Hz [ $=1/(2 \cdot 14 \mu s)$ ], which allowed observation of the full 240-ppm spectrum on one-half of the quadrature transform (i.e., the data along the evolution period  $t_1$  are real only). A file size-limitation in the MSL software allowed a maximum of 1,024 experiments in  $T_1$ , so that  $T = 2 \cdot 14 \mu s \cdot 1024 = 28.7$  ms. For this value of  $T$ , Equation (23) yields  $\nu_{1/2}^t = 15.4$  Hz. We measured a linewidth  $\nu'_{1/2}$  of 20 Hz, which would result [see Equation (22)] if the true linewidth ( $1/2\pi T_2$ ) were 16 Hz. If one assumes a Gaussian rather than Lorentzian line shape, the same 16-Hz true linewidth is computed from the measured  $\nu'_{1/2}$  of 20 Hz.

The first three pulses used in Exps. 1 and 2 are known to generate multiple-quantum (MQ) coherence (Ref. 62, Chap. 5; 76). The dipolar interactions mix states following the first pulse, and this mixing of states allows MQ (mixed  $\Delta m > 1$ ) states to be generated by the second strong pulse. The third pulse then converts some of the MQ coherence back into observable

( $\Delta m=1$ ) coherence, which, when the time period between the second and third pulses is short compared to  $T_2$ , as in our experiments, provides a net positive signal which adds constructively to the normal, single-quantum signal. Thus, the MQ coherence generated during these experiments will lengthen the observed  $T_2^\dagger$  values. This is exactly what is observed;  $T_2^\dagger$  is larger in this case (9.9 ms) than as detected in the echo experiment described below (~6 ms).

These results were confirmed by a second method, i.e., measuring  $T_2^\dagger$  directly in an echo experiment. The  $^{13}\text{C}$  magnetization was generated by cross-polarization, and a single  $\pi$  pulse was applied following a delay  $\tau_e$  after the CP period. The decay of the echo amplitude at  $2\tau_e$  as a function of  $\tau_e$  yields  $T_2^\dagger$ . From this method we find a nonexponential decay, but with a major component that can be characterized by a  $T_2^\dagger$  of about 6 ms, which leads to a  $\nu_{1/2}$  of about 25 Hz.

Finally, in the third method, the  $\pi$  pulses in the echo experiment are applied as a train, as in Exp. 2 (Figure 17). In this case, spin-locking can occur. The average locking field strength is  $H_1 t_w / (2\tau_e)$ , where  $t_w$  is the width of the  $\pi$  pulse and  $H_1$  is the RF field strength, and this spin-locking provides additional heteronuclear decoupling. Thus, with this sequence, we measure a  $T_2^\dagger$  of about 13 ms, which leads to a  $\nu_{1/2}$  of about 12 Hz.

These values for  $T_2^\dagger$  allow us to compare  $^{13}\text{C}$  and  $^1\text{H}$  solid-state NMR imaging. Typically, proton linewidths of solids under multiple-pulse sequences are  $\geq 0.25$  ppm (Ref. 77), and we find that for PEEK and DER/DETA under a dipolar-narrowed-Carr-Purcell (DNCP) sequence (Ref. 78),  $\nu_{1/2} \approx 150$  Hz at 7.0 T. From Equation (19),  $^{13}\text{C}$  imaging should provide somewhat better ultimate resolution capability than  $^1\text{H}$  imaging, on the condition, however, that the  $^{13}\text{C}$  image can be obtained with adequate S/N. From Equation (20), we can see that

$$\frac{(S/N)_{^{13}\text{C}}}{(S/N)_{^1\text{H}}} \geq 0.011 \cdot c_p \cdot \frac{\gamma_{^{13}\text{C}}}{\gamma_{^1\text{H}}} \cdot \left[ \frac{150}{25} \right]^{1/2} \sim 0.03 \quad (21)$$

where  $c_p$  equals the CP enhancement factor of  $\leq 4$ . Even if the  $^{13}\text{C}$  linewidth were as low as 5 Hz,  $^{13}\text{C}$  solid-state imaging would still be considerably

less sensitive than  $^1\text{H}$  solid-state imaging. As discussed below, sensitivity will in fact become a factor of overriding importance in the practical use of (especially  $^{13}\text{C}$ , but also  $^1\text{H}$ ) NMR imaging as an NDE technique.

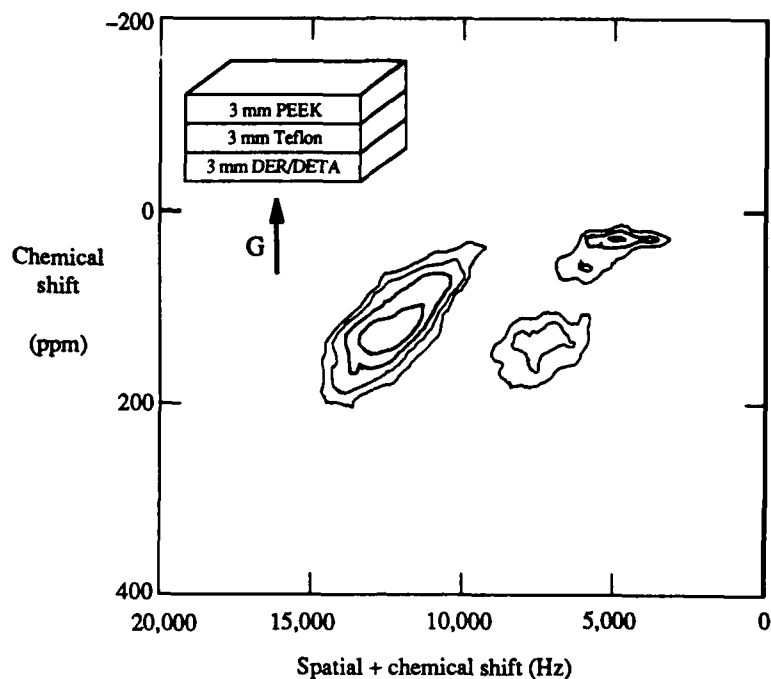
The image shown in Figure 20 was obtained using Exp. 1. Chemical-shift interactions are not refocused in this experiment; during the evolution period,  $t_1$ ,  $^{13}\text{C}$  magnetization evolves under both the gradient and the chemical-shift interactions, whereas during the detection period,  $t_2$  the gradient is off (see Figure 16). This combination of gradient and chemical shift during  $t_1$  causes the canting of the two-dimensional image shown in Figure 20. PEEK and DER/DETA are clearly resolved, with a resolution of  $\sim 0.5$  mm.

Noting that  $\gamma G = 8$  kHz/cm, and  $1/(2\pi T_2^\dagger)$  is about 25 Hz, use of Equation (19) might lead us to expect  $\Delta x \approx 50/8000 = 0.006$  cm (60  $\mu\text{m}$ ) spatial resolution in Figure 20. The resolution was limited, however, by the use of a digital S/N improvement filter. To obtain usable S/N, a 200-Hz line-broadening function was multiplied to the time domain data in both dimensions. Now we see that  $(200 \text{ Hz})/(8,000 \text{ Hz/cm}) = 0.25$  mm, which is close to the observed resolution. Even with this S/N enhancement technique, the experiment took 10.7 h with 400 repetitions for each of the 64 values of the evolution period,  $t_1$ . A repetition time of 1.5 s was used for these experiments; proton  $T_1$  values for these materials are listed in Table 5.

The contours in Figure 20 show one maximum on the left side, due to aromatic carbons of PEEK, and two maxima on the right side, due to aromatic and aliphatic carbons of the DER/DETA epoxy resin (see Figure 18). Clearly, the chemical shift is sufficient to delineate PEEK from DER/DETA, but would most likely not be sufficient to delineate DER/DETA from 3501-6 neat resin. This level of chemical resolution is low in comparison to that obtainable by liquid-sample or MAS solid-state NMR (see Figure 18), but  $^{13}\text{C}$  chemical-shift imaging of static samples could still lead to useful contrasting in certain cases.  $^{13}\text{C}$  NMR imaging of rotating solids has been achieved (Refs. 39-42), where chemical-shift resolution should be greatly enhanced. The sample rotation aspects of these experiments, however, place restrictions and constraints on the sample which negate the practical application of the method except under special circumstances.

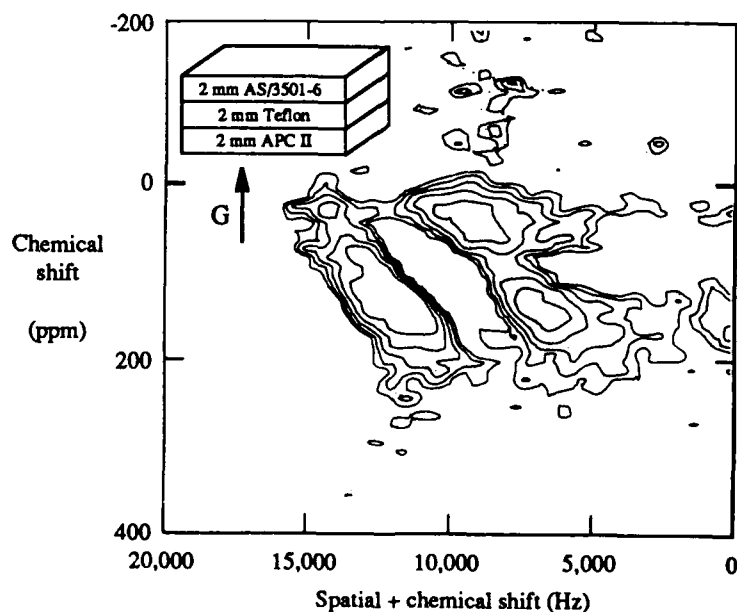
Small samples of APC-II PEEK and AS-4/3501-6 epoxy cross-ply laminates were arranged in the configuration shown in Figure 21, analogous to that





89-221-229

Figure 20.  $^{13}\text{C}$  chemical-shift image of a DER/DETA resin/Teflon/PEEK resin sandwich. Contours step down by multiples of 0.7 from the maximum intensity.

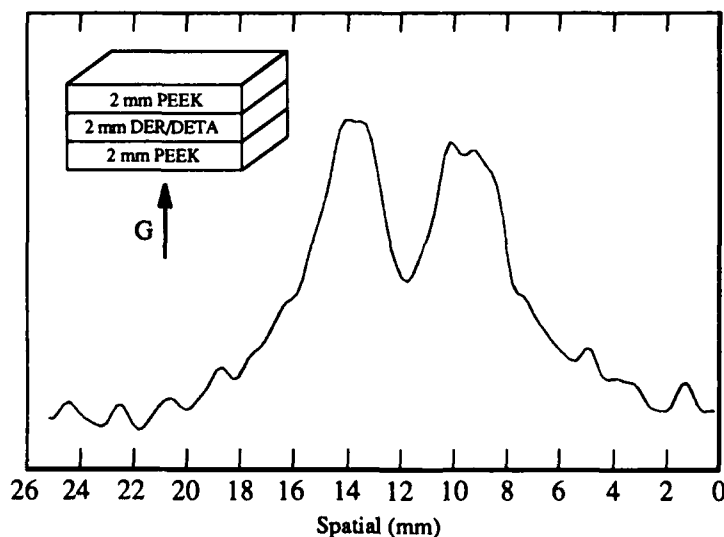


89-221-230

Figure 21.  $^{13}\text{C}$  chemical-shift image of an AS-4/3501-6 laminate/Teflon/PEEK laminate sandwich.

used for the neat resins discussed above. Experiment 1 produced the  $^{13}\text{C}$  NMR image shown in Figure 21. This experiment, requiring 26.7-h, 200-Hz line broadening, was again applied in both dimensions, and resolution and sensitivity are both inferior to those obtained by the shorter experiment presented in Figure 20. This degradation resulted from the reduced resin content ( $\approx 30\%$  by weight) in the laminates and the RF attenuation caused by the conducting carbon fibers (see Section 3.4; Ref. 1).

One of the most promising approaches for obtaining useful NMR images of solids is to combine chemical-shift imaging as discussed above with other contrast approaches. For this purpose, we have explored the use of proton spin-lattice relaxation times of PEEK and epoxy resin (see Table 5) to provide contrast between these materials. Figure 22 shows the image obtained by use of the pulse sequence, Exp. 2, shown schematically in Figure 17. This sequence first inverts the proton magnetization, and then waits until the proton magnetization in the DER/DETA resin is nulled ( $t_{\text{null}} = \ln(2)T_1 = 0.2 \text{ s}$ ) before continuing. With no proton magnetization in the epoxy resin prepared for cross-polarization, a CP  $^{13}\text{C}$  signal of only the PEEK resin is observed. This sequence refocuses chemical-shift interactions during detection, which improves the S/N; thus the experiment took only 2.1 h with the same 200-Hz line broadening applied to the time domain data.



89-221-231

Figure 22.  $^{13}\text{C}$  NMR image of a PEEK resin/DER/DETA resin/PEEK resin sandwich, obtained using  $^1\text{H}$  spin-lattice relaxation as the contrast mechanism.

Similar experiments could be performed using  $T_{CH}$  (the  $^{13}\text{C}$ - $^1\text{H}$  cross-relaxation time),  $T_{1\rho}$  (for  $^{13}\text{C}$  or  $^1\text{H}$ ) or any other temporal NMR parameter that differs from one region or structure to another in the sample being imaged. As discussed previously,  $T_{CH}$  differences among structural components unavoidably affect intensities in the images shown in this work. The aliphatic carbons in the epoxy resin have an optimum contact time (maximum  $^{13}\text{C}$  signal) of  $\sim 400\ \mu\text{s}$ , whereas the aromatic carbons in PEEK are optimally cross-polarized by a 2- to 4-ms contact time (see Table 9). We used a 2-ms contact time to accommodate the lower CP efficiency in PEEK and to enhance the intensity of the broad, aromatic carbons.

An important aspect of these experiments is that it took 2 h to obtain a one-dimensional image, containing a resolution of  $\geq 300\ \mu\text{m}$ . In assessing the future viability of  $^{13}\text{C}$  NMR imaging of solids, it is important to predict the time needed to turn this 2-h experiment into one which would achieve  $100 \times 100\text{-}\mu\text{m}$  resolution within a  $100\text{-}\mu\text{m}$  slice. Assuming we do not increase the field of view of 6 mm of the experiment, which would further increase the experimental time, an accurate estimate for increasing the spatial resolution on the CSU spectrometer (the same experimental conditions as for the 2-h image) can be made as follows. The  $100\text{-}\mu\text{m}$  slice will reduce the volume by approximately 60. Increasing the resolution from 300 to  $100\ \mu\text{m}$  in one dimension requires increasing the S/N in this dimension such that the line broadening of the S/N improvement function can be decreased. This requires about a  $(300/100)^{1/2}$  better S/N. Adding the second dimension again decreases the volume element by  $\sim 60$ . Thus the S/N must be increased by a factor of  $60 \times 60 \times \sqrt{3} = 6235$ , increasing the experiment time, TE, to [see Equation (18)]  $2\ \text{h} \times 6235^2 = 78 \times 10^6\ \text{h} = 3 \times 10^6\ \text{days}$ . We can foresee a tenfold improvement in S/N by increasing the static magnetic field strength (this is only possible with superconducting magnets which will limit the size of the sample to  $\leq 1\ \text{m}$  in two directions), and perhaps a threefold improvement with an optimized probe design. Even with these improvements, the experiment would take  $3 \times 10^6 / (30^2) = 3,600\ \text{days}$ . Resolution of  $200 \times 200\ \mu\text{m}$  with a slice thickness of  $500\ \mu\text{m}$  would still take 9 days, and this is with a relatively small field of view of  $< 10\ \text{mm}$ . Thus, we see that practical, high-resolution, three-dimensional NMR imaging of solid-state materials using  $^{13}\text{C}$  may never be achievable. Equation (24), on the other hand, shows that  $^1\text{H}$  images would take  $\sim 0.001$  as long as  $^{13}\text{C}$  images, making

high-resolution NMR imaging of solids by use of  $^1\text{H}$  realizable. Our own experience confirms the practicality of  $^1\text{H}$  imaging of solid-state materials.

$^{13}\text{C}$  NMR imaging will almost certainly remain a tool for the research laboratory, where experimental times can remain large, fields of view small, and spatial resolutions relatively large. Moreover, there must be a specific reason, almost certainly some contrast mechanism unattainable with  $^1\text{H}$  due to the strong proton spin-bath interactions, for pursuing  $^{13}\text{C}$  imaging in solids.

The three images shown in Figures 20, 21, and 22 clearly demonstrate the ability to obtain  $^{13}\text{C}$  NMR images of solid polymeric materials, including small carbon-fiber laminates, using chemical-shift and spin-lattice relaxation as contrast mechanisms. We expect that improvements in resolution and sensitivity will be made in the future, as additional attention is focused in this direction. Consideration of the less-stringent requirements of heteronuclear decoupling versus multiple-pulse homonuclear decoupling, and the ability to manipulate the carbons via contact time, dipolar dephasing, either  $^1\text{H}$  or  $^{13}\text{C}$  relaxation times, and chemical shift, suggests that  $^{13}\text{C}$  solid-state NMR imaging may become useful for the nondestructive study of solid materials, especially in the research arena where data-acquisition time, fields of view, and spatial resolution are not overriding factors.

### 3.7 $^1\text{H}$ NMR Line-Narrowing and Imaging Studies\*

We undertook the design of a  $^1\text{H}$  NMR imaging experiment that would use the relatively immobile protons in OMC materials for detection with the following specific goals:

1. Image samples of a general shape and size, with the following requirements:
  - a) Exclude from consideration sample rotation (Refs. 39-42), which reduces chemical-shift anisotropy and field inhomogeneity effects.
  - b) Plan for the eventual use of a permanent or electromagnet design, with gaps to allow samples of infinite length in two directions (which necessarily means static magnetic-field strengths will be at most 2 T).

---

\* Much of this work is published in Ref. 45.

- c) Allow for the eventual use of optimized coil designs similar to surface coils.
- 2. Design an imaging experiment that would utilize multiple-pulse decoupling for  $^1\text{H}$  line-narrowing, and would
  - a) optimize S/N (maximize decoupling efficiency, minimize gradient switching times),
  - b) optimize spatial resolution (allow use of maximum field gradient strengths),
  - c) minimize artifacting (allow controlled volume selection having good RF homogeneity across the whole volume; use a decoupling scheme which minimizes error terms, especially cross terms involving frequency offset), and
  - d) allow for controlled slice selection (requiring a new pulse sequence).

The first area investigated relates to items 2.a and 2.c above, i.e., choosing which homonuclear decoupling scheme to integrate into an imaging experiment. Many homonuclear decoupling schemes exist in the literature (Refs. 48,49,72). We quantified the decoupling efficiency of a select number of these schemes which were best suited for NMR imaging. These schemes included the MREV-8, DNCP, BR-24, and BR-52 sequences. We also looked at the efficiency of a BR-24 sequence modified to allow for quadrature detection. The decoupling efficiency is directly related to  $T_2^\dagger$  (the observed magnetization decay time during decoupling), and values observed on PEEK and DER/DETA were all equivalent ( $\sim 160 \mu\text{s}$ , arising from chemical-shift anisotropy), as expected, since these sequences are nearly identical except for their artifacting. The modification used to turn the MREV-8 sequence into the DNCP sequence can be performed similarly with the BR sequences, and this modification gives improved results in all cases ( $T_2^\dagger \approx 1 \text{ ms}$ ) because of the removal of chemical-shift anisotropy, field inhomogeneity, and susceptibility effects.

The MREV-8 scheme currently gives minimum artifacts during quadrature detection (in other work, we have developed a scheme for quadrature detection with the BR-24 sequence; Ref. 79). Quadrature detection is necessary because all multiple-pulse decoupling schemes work over a limited frequency

interval,  $\Delta F_{MP}$ , which limits the field of view, FOV:

$$FOV = \frac{\Delta F_{MP}}{\gamma G} \quad (22)$$

Most multiple-pulse schemes work only over a maximum of  $\pm 10$  kHz, so that with the application of  $\gamma G = 50$  kHz/cm (a moderate field gradient strength), the FOV equals 2 mm with nonquadrature detection. Note that if one lessens  $\gamma G$  to increase the FOV, the spatial resolution will be degraded:

$$\Delta x \approx \frac{\Delta \nu}{\gamma G} = \frac{(FOV)(\Delta \nu)}{\Delta F_{MP}} \quad (23)$$

where  $\Delta \nu = 1/(\pi T_2^{\dagger})$  is the narrowed linewidth during the decoupling sequence.

Another important aspect which bestows additional importance to quadrature detection pertains to Nyquist's theorem. The simplest approach to using a multiple-pulse sequence is to observe signal in only the first window of each multiple-pulse cycle. A simple modification is to observe another point midway in the cycle. In this detection mode, the information is nonquadrature, and the sweep width is limited by the cycle time and Nyquist's theorem, as shown in Table 10. The sweep widths obtained with nonquadrature detection schemes are most likely too small to allow for both adequate FOV and  $\Delta x$ , thus detection schemes that use every window within a multiple pulse experiment, which widens the sweep width, are necessary. Our experience shows that the longer cycles incurred with BR sequences lead to larger artifacts than with the shorter MREV-8 sequence (Refs. 79,80). The MREV-8 sequence with quadrature detection doubles the FOV for any particular  $\Delta x$  and minimizes artifacting; therefore, we have used MREV-8 sequences for this portion of the work.

Table 10. Sweep widths obtainable from multiple-pulse sequences with various detection schemes.

Sequence	Cycle time	Sweep width for $\tau = 4 \mu s$	
		Detect twice per cycle	Detect in every window
MREV-8	$12 \tau$	20.8 kHz	$\pm 20.8$ kHz
BR-24	$36 \tau$	6.9	$\pm 20.8$
BR-52	$78 \tau$	3.2	$\pm 20.8$

89-221-238a

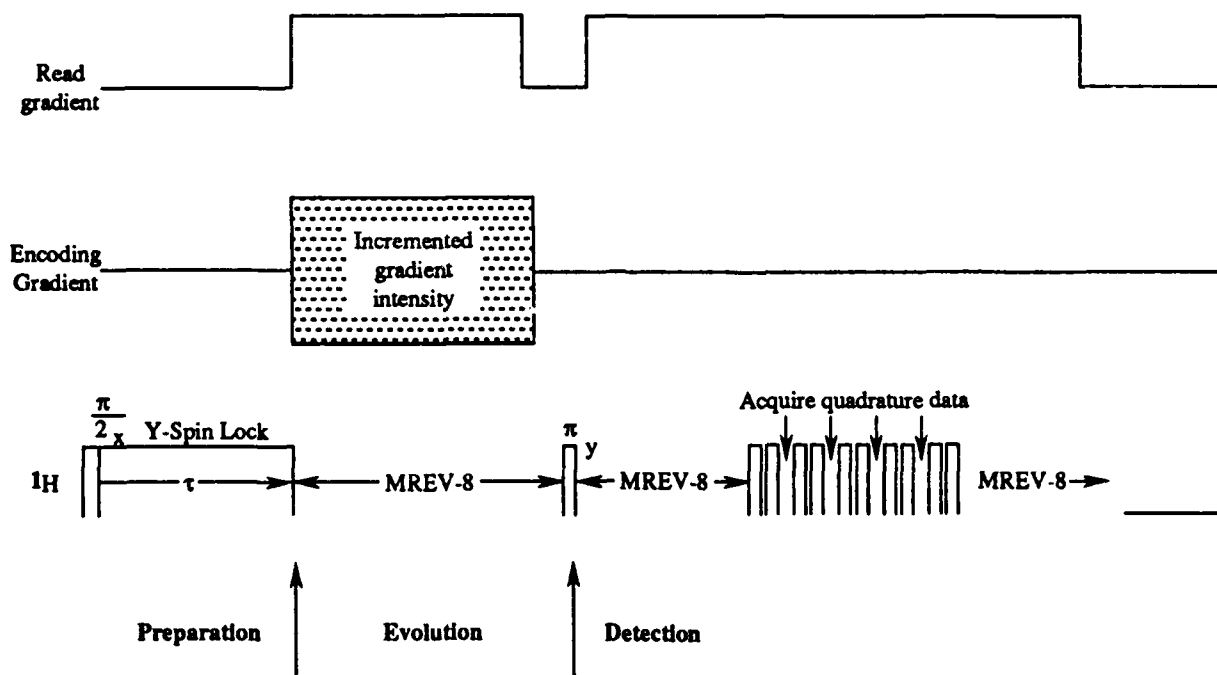
The MREV-8 sequence provides adequate decoupling provided sufficient transmitter power is available; we assume this to be the case initially, but keep in mind that the BR sequences are better when the availability of transmitter power is reduced. To use BR sequences, it is necessary that at least every other window be used, and we are currently working on methods to reduce artifacting caused by this type of data acquisition.

We did not consider incorporating multiple quantum schemes (Refs. 9,10) into the NMR imaging experiment for two reasons:

1. Currently, there is no method for selectively exciting a particular quantum transition with intensities approaching even an order of magnitude less than normal, single-quantum schemes (Refs. 9,10,62,76), and, as we have discussed many times, it is of paramount importance to keep the S/N as large as possible.
2. The introduction of very large magnetic field gradients (Ref. 36) makes the previous reasoning of producing MQ in order to achieve mG gradients (m is the quantum order; Ref. 62) no longer practical; the more practical approach is simply to incorporate field gradient coil designs that provide larger magnetic-field gradients.

Using the MREV-8 sequence, we developed the imaging experiment shown schematically in Figure 23. This experiment uses the encoding and read gradients in a manner similar to many liquid MRI experiments (Ref. 62). Maximum field gradient strengths are achieved, which maximizes the achievable spatial resolution [see 2.c above and Equation (23)]. This experiment also allows for simple control of the gradients, and for fast gradient switching. The gradients on the MSL, when properly set up, switch in about 100  $\mu$ s, whereas most gradient systems switch in >1 ms. Fast gradient-switching is an essential feature in NMR imaging experiments involving solid materials. Longer switching times require a storage period, which reduces S/N significantly and complicates the experiment and data analysis (Refs. 3,27). Any homonuclear decoupling scheme which does not refocus linear  $I_z$  interactions can replace the MREV-8 sequence. The  $\pi$  pulse in the middle of the sequence refocuses chemical-shift effects and other linear  $I_z$  interactions.

By use of the experiment in Figure 23, we obtained the images shown in Figure 24. The preparation portion of the experiment is the contrast prep-



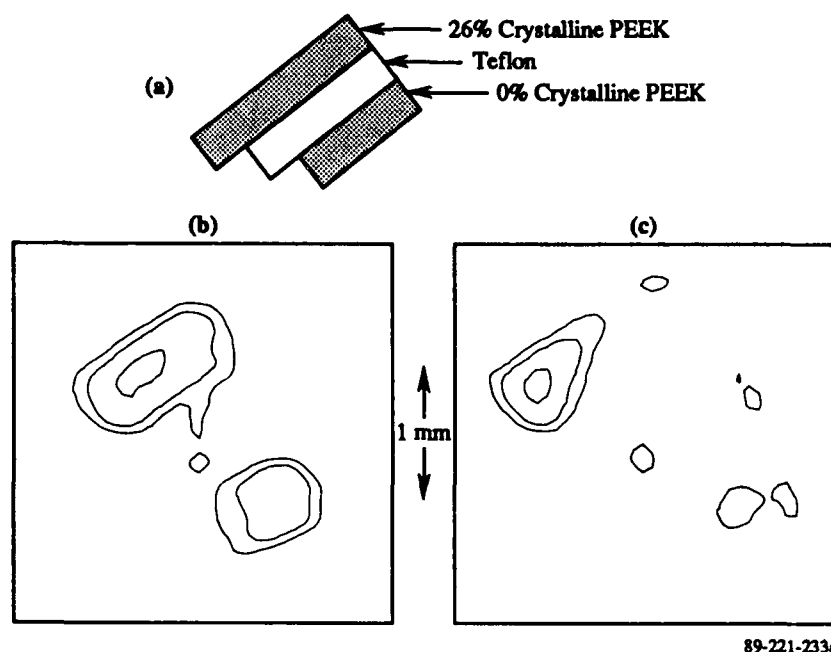
89-221-232

Figure 23. Schematic of  $^1\text{H}$  NMR imaging experiment.

eration period of Figure 1, and is designed to contrast the crystallinity in PEEK using the different  $T_{1\rho}(^1\text{H})$  observed (see Section 3.2) for crystalline and amorphous phases in this material. The evolution and detection periods are designed as described above to optimize S/N and spatial resolution, and to minimize artifacting. As the spin lock time,  $\tau$ , is increased in the preparation period, the magnetization in the amorphous regions decays faster than in the crystalline regions, and we observe a decreasing ratio of intensities occurring from the 26% crystalline sample with respect to the ~0% crystalline sample, as shown in Figure 24. The volume ratios are plotted in Figure 25, along with the predicted volume-ratio dependence on  $\tau$  shown as the curve, derived from the  $T_{1\rho}(^1\text{H})$  values found during the work described in Section 3.2.

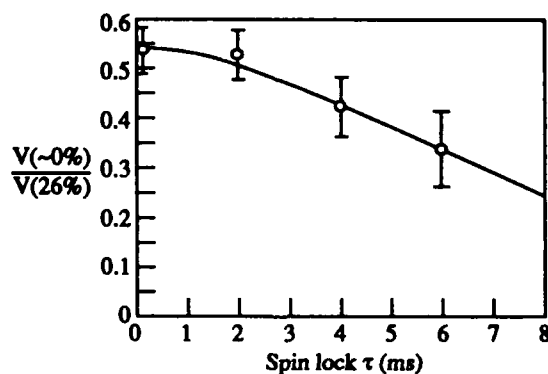
The spatial resolution observed in these experiments is  $\sim 250 \mu\text{m}$ , with  $\gamma G$  equaling 70.4 kHz/cm. The resolution is limited by chemical-shift anisotropy, where  $\Delta\nu = 2,000 \text{ Hz}$  is observed during the MREV-8 sequence. Time-varying gradient schemes (Ref. 27), which would allow application of DNCP (Ref. 78) or refocused gradient imaging (Refs. 31,32) schemes, might improve the spatial resolution even with smaller applied  $\gamma G$  values since these schemes remove the chemical-shift anisotropy effects. Much larger, static, linear gradients have now become available (Ref. 36), up to  $\gamma G$





89-221-233a

Figure 24.  $^1\text{H}$  NMR images of PEEK sections having 26% and ~0% crystallinities: (a) schematic of sample used, (b) image with  $\tau = 0$  ms, (c) image with  $\tau = 6$  ms.



89-221-234a

Figure 25. Ratio of volume of ~0% to 26% crystalline PEEK regions for various spin-lock times  $\tau$ . The curve shows a fit to the data consistent with measured  $T_{1\rho}$  ( $^1\text{H}$ ) values.

= 2,000 kHz/cm for  $^1\text{H}$ , so straightforward application of our technique should allow 1- $\mu\text{m}$  resolution, provided that sufficient S/N is obtained from each voxel (which is presently unlikely for <10- $\mu\text{m}$  resolutions; still, we prefer being limited by sensitivity rather than by the ultimate resolution capability). Aspects and comparisons of various  $^1\text{H}$  imaging experiments are provided in Section 4.0.

The experiments presented in this section have demonstrated the viability of  $^1\text{H}$  NMR imaging as a potential technique for NDE of aerospace materials. Some technical advances are still required, however, before the technique can become truly practical. First, addressing criterion 2.d above, a method for selecting slices in the sample in a controlled manner needs to be developed. One promising technique has recently been introduced (Ref. 33), and this or some similar approach will almost certainly be found to be of practical use soon. Second, addressing criterion 2.c above, the susceptibility of multiple-pulse sequences to artifacts currently remains a serious problem. More experience and better probe designs may reduce this susceptibility, but the development of a new multiple-pulse scheme which is effective over a larger frequency bandwidth ( $> \pm 10$  kHz) and is concurrently less susceptible to artifacts, especially those generated by quadrature detection, would be most desirable.

If an NMR image could be obtained without using line narrowing (i.e.,  $T_2^\dagger \leq 20 \mu\text{s}$ ), many technical requirements of the experiment would be simplified. A method for achieving such an image is backprojection-reconstruction (Refs. 34,62,81). Assuming that we need to achieve  $\Delta x = 0.01$  cm resolutions in at least one spatial direction (e.g., across the plies), the FOV is

$$\text{FOV} = \frac{\text{SW}}{\gamma G} = \text{SW} \cdot \Delta x \cdot \pi T_2^\dagger \leq \text{SW}(\text{Hz}) \cdot 6 \times 10^{-7} \text{ cm}, \quad (24)$$

where SW is the sweep width used for detection. Thus, a FOV of 2 cm (assuming 256 pixels are wanted along each dimension) would require a SW of 3 MHz, which is barely feasible. For a more practical SW of 1 MHz (which also improves the S/N), the FOV would be 6 mm. This FOV value should be compared with the  $\sim 1$ -cm FOV obtainable by use of multiple-pulse line-narrowing techniques, where  $T_2^\dagger \approx 1$  ms but  $\text{SW} \leq 40$  kHz (here the SW is limited by the digital acquisition rate, not the receiver bandwidth; see Table 10). The complete SW in either case would not be usable, limiting the effective FOV even more, but the backprojection-reconstruction method assumed above requires the use of a  $\gamma G = 1.6$  MHz/cm, which is very large. Multiple-pulse line-narrowing techniques appear to be necessary features, perhaps combined with backprojection-reconstruction methods, but still necessary, for the practical application of  $^1\text{H}$  NMR imaging to solid materials.

#### 4.0 ASSESSMENT OF NMR AND NMR IMAGING FOR THE NONDESTRUCTIVE EVALUATION OF COMPOSITE MATERIALS

To accurately assess NMR and NMR imaging, let us first reconsider the general requirements for application of NMR spectrometry to the NDE of composite systems. The following list forms a basis of criteria for such application of an NMR spectrometer:

- i) The large sizes of aerospace components that would be studied (e.g., a wing-skin) require the use of permanent magnets or electromagnets which allow infinite sample dimensions in two directions. Such magnets are limited in field strength to  $\leq 2.1$  T (90 MHz for  $^1\text{H}$ ).
- ii) The large sizes of aerospace components require use of surface coils in the NMR experiments.
- iii) Detection of solvent effects in composite materials, e.g., for water or jet fuel, can be performed with moderate magnetic-field gradients and gradient switching times. Simple modifications of the RF design and data-acquisition systems from MRI spectrometer designs might be necessary. These requirements would be easily satisfied by a spectrometer capable of imaging the more immobile resin matrix materials, as discussed next.
- iv) Invasive fluids do not appear to be a viable avenue for the NMR imaging of features in aerospace OMC materials, as discussed in Section 3.5. Thus, solid-state imaging techniques become necessary for evaluating flaws such as voids; delaminations; fiber content, breakage, and orientation; catalyst content; crosslink density or percent crystallinity; and chemical composition of the matrix material (e.g., composition of unreacted chain-ends).

Solid-state NMR imaging capability requires the following:

- a) large magnetic-field gradients (2 mT/cm should be sufficient) capable of fast ( $\leq 100$ - $\mu\text{s}$ ) switching,
- b) strong (1 kW), fast (0.2- $\mu\text{s}$  rise and fall time) RF transmitters, capable of generating a 90-degree RF pulse length of  $\leq 5$   $\mu\text{s}$  in any portion of the sample,
- c) nominal detection speeds (4  $\mu\text{s}$  per point), but with wide receiver bandwidths ( $\geq 1$  MHz) and stroboscopic triggering capability, and

- d) optimized probe designs making use of surface coils for highest possible signal-to-noise (high Q) while also having sufficiently short ring-down ( $\sim 4\text{-}\mu\text{s}$ ) times.
- v) The experimental design should also be flexible enough to allow an accurate assessment of the remaining most likely candidates for NDE studies, including
  - a) fast detection ( $0.1\text{ }\mu\text{s}$  per channel),
  - b) time-varying gradients to allow the investigation of refocused gradient (Refs. 31,32) and similar imaging experiments,
  - c) computer-controlled transmitter power to allow for the investigation of slice selection by rotating-frame RF gradients (Refs. 30,33),
  - d) precise computer-controlled field gradient rotation of very large field gradients to allow the investigation of backprojection-reconstruction techniques (Refs. 34,65,86), and
  - e) multinuclear capability to allow the investigation of  $^{13}\text{C}$  NMR imaging (Refs. 2-4) and other nuclei contained in catalysts (e.g.,  $^{11}\text{B}$ ) and matrix additives (e.g.,  $^{27}\text{Al}$ ; Ref. 34).

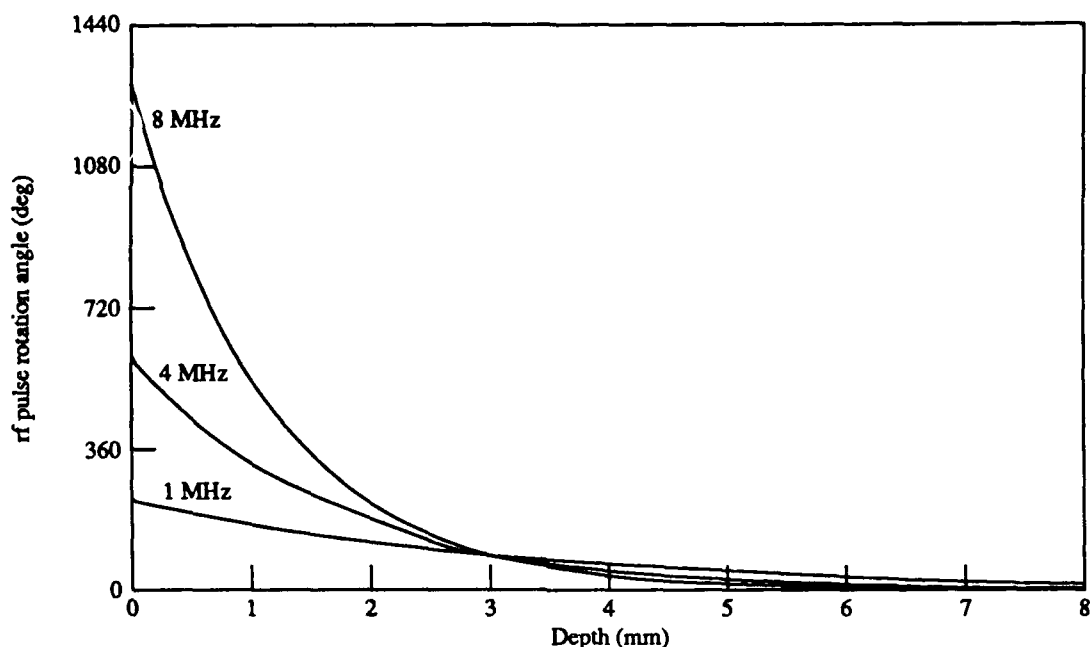
In the previous sections of this report, we clearly demonstrated the viability of  $^1\text{H}$  and  $^{13}\text{C}$  NMR imaging of solid materials, and discussed some of the limitations and technical advances still needed to make these techniques truly practical. For nonlossy samples (i.e., samples not containing carbon fibers), our current MSL spectrometer has adequate RF generation and detection capabilities to satisfy requirements iii and iv, and only simple modifications would be required to enable the MSL to satisfy requirement v. Meeting requirement i needs only interfacing the MSL to an electromagnet, a simple task, whereas attainment of requirement ii is straightforward. Thus, for noncarbon-fiber-containing systems, we have the capability and are currently pursuing NMR and NMR imaging of solid materials for practical NDE of aerospace composites.

An assessment of these techniques for the NDE of OMC containing long carbon fibers must, however, be based on considerations of the interaction of the fibers with the RF electromagnetic fields, as discussed in Section 3.4. With any nominal NMR approach, RF is first applied to the sample in microseconds- to millisecond-length pulses, after which the induced RF from the sample must be detected. As shown in Table 8 and described by Equations

(5)-(12), the ability of the RF fields to penetrate the sample depends on the applied static magnetic-field strength (which determines the RF frequency for a particular nucleus, and also affects the sensitivity), and the sample makeup, geometry, and orientation in the RF field. In Section 3.4, it was demonstrated that NMR and NMR imaging of a large OMC structure containing carbon fibers are not feasible for static magnetic-field strengths greater than 0.25 T ( $\nu = 10$  MHz). Thus, we consider the possibility of lowering the magnetic field strength, and assess the effect of the lower field strengths on the design and capabilities of an NMR imaging spectrometer.

First, we must consider in more detail what might be the optimum magnetic field strength to use. At this point, we assume that flaws within a large cross-ply laminate having a minimum thickness of 1/4 inch ( $\sim 6$  mm) need to be detected. Figure 10 shows the transmitter power density required to produce a 5- $\mu$ s, 90-degree RF pulse (to satisfy requirement iv.b) as a function of depth in a cross-ply laminate. The calculation is shown for propagation of the RF perpendicular to the ply orientations (a worst-case scenario, but necessary for NDE of large structures such as wing-skins). To detect a flaw at the center of the laminate at  $\sim 3$  mm, the transmitter power required at 8 MHz is 2.5 kW/cm<sup>2</sup>. This power exceeds typical transmitter and probe circuit capacities. From this information, we confine the design to building a spectrometer having an operating frequency of  $\leq 8$  MHz.

The RF attenuation produces other potential problems which the spectrometer design should attempt to avoid. Figure 26 shows the RF pulse rotation angle [see the discussion surrounding Equation (12)] which changes as a function of depth due to the RF attenuation in cross-ply samples having the same orientation as for Figure 10. The change in rotation angles can be used for volume selection in an imaging experiment (as in rotating frame imaging, Refs. 30,33,62), such that the volume around 3-mm depth where the rotation angle equals 90 degrees is selected in the experiment. Other volumes, however, particularly at rotation angles of 270, 450, 630 ... degrees will almost certainly also be selected at the same time, and will produce artifacts that may be difficult or impossible to deal with. Since the rotation angles do not reach 270 degrees at 1 MHz, these artifacts are sure to be reduced at this frequency. As the frequency is raised from 1 MHz, an exponentially growing number of 270, 450, 630 ... degree points



89-221-235b

Figure 26. The RF pulse rotation angle as a function of depth in cross-ply carbon fiber composites with the RF propagation perpendicular to the plies (along  $\theta = 180^\circ$ ) when a 90-degree rotation occurs at 3 mm. Curves are drawn at 1, 4, and 8 MHz.

will occur in the sample, and experiments will become difficult to perform. Some scheme to negate these problems can probably be devised, but the added complexity, perhaps with loss in S/N, will be undesirable.

From these considerations, it would appear that a spectrometer designed about an RF frequency of 1 MHz (a 23.5-mT static magnetic-field strength for detecting  $^1\text{H}$ ) is optimum, with any increase in frequency not to exceed 8 MHz. With this fundamental input, we can now estimate other parameters of importance to NMR and NMR imaging of OMC materials. As we have discussed previously, the S/N ratio is one such parameter. To estimate the S/N, we use the following approximate relationships (see also the discussion surrounding Equation (13) and footnote at bottom of page 31).

$$S/N \propto (Q/T_1)^{1/2} H_o^{3/2} A \quad (25)$$

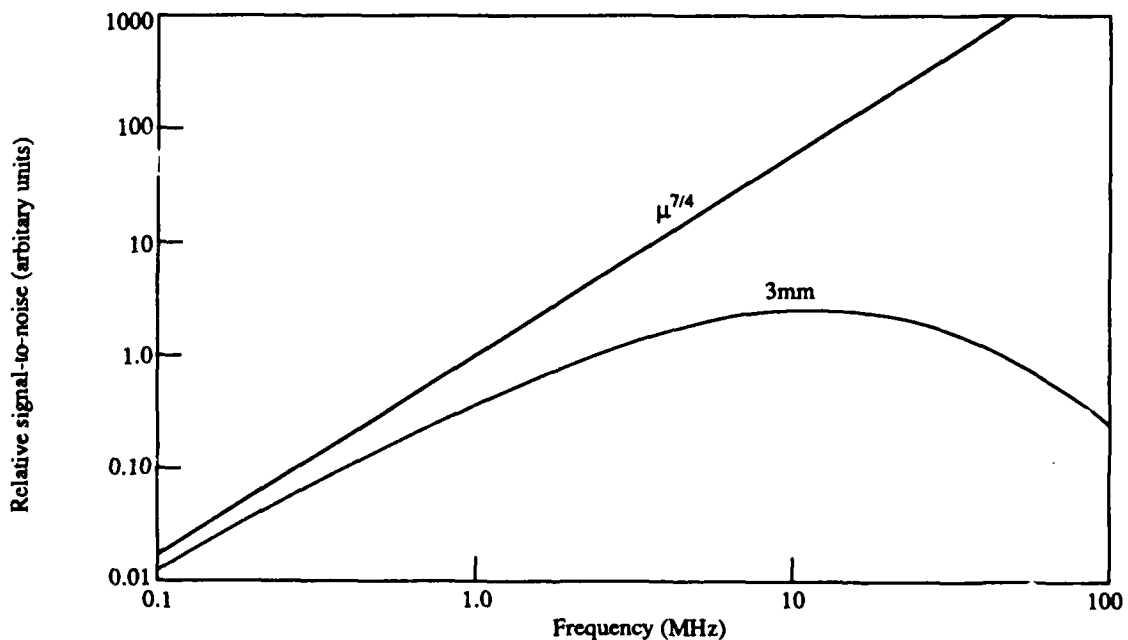
and  $\nu_o \propto H_o$

where  $H_o$  is the static magnetic-field strength,  $T_1$  is the spin-lattice relaxation time of the nuclei at  $H_o$ ,  $Q$  is the quality factor of the probe,  $\nu_o$  is the observation frequency, and  $A$  is the RF attenuation factor.  $Q$  must

decrease approximately in proportion to the frequency, i.e.,  $Q \propto \nu_o$ , so that the detector can respond quickly enough to observe solid-state signals (see discussion below).  $T_1$  in polymers is observed empirically to decrease at most as  $\nu_o^{1/2}$  over the range 100 MHz to 1 MHz (Ref. 82). Combining these approximate expressions gives

$$S/N \propto \nu_o^{7/4} A \quad (26)$$

where  $A=1$  for nonlossy materials, and  $A = \exp\{-d[\pi\nu_o\mu_o\sigma]^{1/2}\}$  for cross-ply laminates as shown in Section 3.4. Equation (26) is plotted in Figure 27 as a function of frequency at a depth  $d = 3$  mm. The difference between this function and that shown in Figure 11 is that here the experimental parameters,  $T_1$ , and  $Q$ , are factored into the  $S/N$ . For  $S/N$  with cross-ply laminates 10 MHz is optimum, but transmitter requirements exclude the use of this high of a frequency. At 1 MHz,  $S/N$  is reduced only by a factor of  $\sim 10$  compared to the  $S/N$  at 10 MHz for laminates, but is about a factor of 1,000 less than the  $S/N$  of nonlossy materials (i.e., nominal NMR) at 85 MHz.



89-221-236b

**Figure 27.** The relative signal-to-noise, including  $Q$  and  $T_1$  dependencies, as a function of frequency at a depth of 3 mm. The straight line is the projected  $S/N$  for a nonlossy material, whereas the curved line is for a cross-ply carbon fiber composite with RF propagation perpendicular to the plies (along  $\theta = 180^\circ$ ).

Thus, an NMR imaging experiment performed at 1 MHz on a large cross-ply composite sample might take  $10^6$  times longer than at 85 MHz of a non-lossy sample to obtain equivalent S/N.

Even if the estimate of  $10^6$  is off by some orders of magnitude, S/N issues clearly will be a limiting factor at frequencies of  $\leq 8$  MHz. The application of superconducting quantum interference devices (SQUIDS) as receivers in these experiments might help alleviate such problems. SQUIDS have been used in NMR experiments run at low frequencies (Refs. 83,84), where the S/N of the SQUID receiver as compared to a conventional receiver is much better at low frequencies and for solid materials which have small  $T_2$  values (Ref. 84):

$$\frac{S/N_{SQ}}{S/N_{con}} \propto \left[ \frac{T_1}{\nu_o T_2} \right]^{1/2} . \quad (27)$$

High-temperature superconductors may enhance the use of SQUIDS for such applications (Ref. 85).

Assuming adequate S/N can be obtained, a closer look at Q is important at this point. Lowering Q allows the circuit to respond more quickly to the RF signals, and since solid-state  $T_2$  values (the characteristic signal decay times) are short, optimized Q values are critical in solid-state NMR. To quantitatively describe and predict this effect, the following relationships are used.  $Q \approx \nu_o / BW$  (Refs. 72,86), where BW is the bandwidth of the circuit. The response time of a circuit  $t_r \approx 2Q/3\nu_o = 2/(3BW)$  (Ref. 87). In solid-state NMR, a common rule-of-thumb is to have  $50t_r \leq 10 \mu s$  (Ref. 87), whereas for multiple-pulse decoupling experiments,  $t_r \leq 0.1 \mu s$  may be needed. Thus, the  $BW \geq 3$  MHz. A 3-MHz BW is impossible at  $\nu_o = 1$  MHz. From this standpoint, going to higher frequencies is better. As discussed in Section 3.7, backprojection-reconstruction techniques might ease the requirements of receiver bandwidth somewhat, but at a cost of needing very high  $\gamma G$  values and probably losing some S/N. Higher frequencies are better also in terms of S/N, but may lead to rotation angle problems as discussed in reference to Figure 26. Considering the seriousness of the approximations used for this assessment, we will need experimental confirmation to better define the relative merits and problems of the possible range of field strengths. A likely result with any attempt is the discovery that



adequate S/N cannot be obtained to achieve practical NMR imaging.

In summary, the only possible avenue for performing practical NDE of OMC samples containing long conducting carbon fibers by use of NMR and NMR imaging appears to require the use of low-frequency rf. An NMR spectrometer that would allow a further assessment of the technique has the following design items:

- i) an electromagnet operating at  $\leq 0.2$  T (8 MHz) for  $^1\text{H}$  NMR, 0.1 T (4 MHz) perhaps being optimum, which can be increased so other nuclei can be studied at the same frequency (e.g., observe  $^{27}\text{Al}$  at 4 MHz with a field strength of 0.36 T);
- ii) a 10-kW transmitter with active Q-spoiling to achieve fast RF pulse rise and fall times, having computer controlled power output (i.e., 10-kW stage is linear, with a controlled power input);
- iii) a receiver circuit, separate from the transmitter circuit, and designed for minimum mutual inductance between the two circuits, making use of surface coil designs, possibly a SQUID detection scheme, and having a bandwidth of  $\geq 3$  MHz;
- iv) fast switching, large-amplitude, magnetic-field gradient designs capable of being time-varied and rotated; fast gradients may be impossible with carbon-fiber-containing laminates as eddy currents might become significant within the laminate; backprojection-reconstruction used in combination with line-narrowing schemes may ease the requirement for fast gradient switching, and;
- v) fast data-acquisition (up to 0.1 MHz per channel), with wide bandwidths ( $\geq 1$  MHz).

The spectrometer designed above would have the limitations of low S/N (much longer data-acquisition times needed than those shown in this report, unless a SQUID is incorporated) and most likely a capability of detecting flaws in OMC throughout a maximum of a 1/4-inch panel thickness.

## REFERENCES

1. A. C. Lind, C. G. Fry and C. H. Sotak, Measured Electrical Conductivities of Carbon-Fiber Composite Materials: Effects on Nuclear Magnetic Resonance Imaging, J. Appl. Phys. (accepted).
2. C. G. Fry, A. C. Lind, M. F. Davis, D. W. Duff and G. E. Maciel, Chemical Shift and Relaxation as Contrast Mechanisms for  $^{13}\text{C}$  NMR Imaging in the Solid State, J. Magn. Reson. 83, 656 (1989).
3. N. M. Szeverenyi and G. E. Maciel, NMR Spin Imaging of Magnetically Dilute Nuclei in the Solid State, J. Magn. Reson. 60(3), 460-6 (1984).
4. G. E. Maciel and M. F. Davis, NMR Imaging of Paramagnetic Centers in Solids via Dynamic Nuclear Polarization, J. Magn. Reson. 64(2), 356-60 (1985).
5. P. Mansfield and P. K. Grannell, "Diffraction" and Microscopy in Solids and Liquids by NMR, Phys. Rev. B 12(9), 3618 (1975).
6. P. Mansfield and P. K. Grannell, NMR 'Diffraction' in Solids?, J. Phys. C 6, L422 (1973).
7. R. A. Wind and C. S. Yannoni, Selective Spin Imaging in Solids, J. Magn. Reson. 36(2), 269-72 (1979).
8. R. A. Wind and C. S. Yannoni, Spin Imaging in Solids Using an NMR Spectrometer, Eur. Pat. Appl. EP 26265, 8 Apr 1981, 13 pp. (1981).
9. A. N. Garroway, J. Baum, M. G. Munowitz, and A. Pines, NMR Imaging in Solids by Multiple-Quantum Resonance, J. Magn. Reson. 60(2), 337-41 (1984).
10. J. Baum, A. N. Garroway, M. Munowitz, and A. Pines, Multiple-Quantum NMR in Solids: Application to Spin Imaging, Congr. AMPERE Magn. Reson. Relat. Phenom., Proc., 22nd, 536-7 (1984). K. A. Mueller, R. Kind, and J. Roos, eds., Zurich Ampere Comm, Zurich, Switz.
11. B. H. Suits and David White, NMR Imaging in Solids, Solid-State Commun. 50(4), 291-5 (1984).
12. B. H. Suits and D. White, Nuclear Magnetic Resonance Imaging of Temperature Profiles, J. Appl. Phys. 60(10), 3772-3 (1986).
13. S. Emid and J. H. N. Creyghton, High Resolution NMR Imaging in Solids, Physica B+C (Amsterdam) 128(1), 81-3 (1985).

14. F. De Luca and B. Maraviglia, "Magic-angle" NMR Imaging in Solids, *J. Magn. Reson.* 67(1), 169-72 (1986).
15. F. De Luca, C. Nuccetelli, B. C. De Simone, and B. Maraviglia, NMR Imaging of a Solid by the Magic-Angle Rotating-Frame Method, *J. Magn. Reson.* 69(3), 496-500 (1986).
16. H. M. Cho, C. J. Lee, D. N. Shykind, and D. P. Weitekamp, Nutation Sequences for Magnetic Resonance Imaging in Solids, *Phys. Rev. Lett.* 55(18), 1923-6 (1985).
17. P. J. McDonald, J. J. Attard, and D. G. Taylor, A New Approach to the NMR Imaging of Solids, *J. Magn. Reson.* 72, 224-9 (1987).
18. W. P. Rothwell, D. R. Holecek, and J. A. Kershaw, NMR Imaging: Study of Fluid Adsorption by Polymer Composites, *J. Polym. Sci., Polym. Lett. Ed.* 22, 241 (1984).
19. W. P. Rothwell, P. N. Tutunjian, and H. J. Vinegar, "NMR Imaging: Nonmedical Applications" in New Directions in Chemical Analysis, Bernard L. Shapiro, ed. (Texas A&M Univ. Press, College Station, TX, 1985), 366-395.
20. S. Blackband and P. Mansfield, Diffusion in Liquid-Solid Systems by NMR Imaging, *J. Phys. C* 19(2), L49-L52 (1986).
21. P. O. Frickland, Materials Applications of Medical Magnetic Resonance Imaging Techniques, in Proc. 18th International SAMPE Tech. Conf., Oct. 7-9, 1989, p. 876-887.
22. D. S. Kupperman, H. B. Karplus, R. B. Poeppel, W. A. Ellingson, H. Berger, C. Robbins, and E. Fuller, "Application of NDE Methods to Green Ceramics: Initial Results," in Proc. Conf. on Applications and Development of NDE for Use in Materials Processing, Am. Soc. Metals, Oct. 5, 1983, Philadelphia, PA, p. 1-13.
23. L. B. Welsh, S. T. Gonczy, J. Dworkin, and A. Giambalvo, Proton NMR Imaging of Green State and Partially Sintered Ceramics, in Review of Progress in Quantitative Nondestructive Evaluation, June 1985, Williamsburg, VA (Plenum Press, NY, 1985) 332.
24. J. L. Ackerman, W. A. Ellingson, J. A. Koutcher, and B. R. Rosen, Development of Nuclear Magnetic Resonance Imaging Techniques for Characterizing Green-State Ceramic Materials, in Proc. 2nd Intl.

Symposium on the Nondestructive Characterization of Materials,

Montreal, Canada, July 21-23, 1986.

25. L. B. Welsh, S. T. Gonczy, R. T. Mitsche, and L. J. Bauer, Proton NMR Imaging of Green State Ceramics, in Review of Progress in Quantitative Nondestructive Evaluation, vol. 6A, D. O. Thompson and D. E. Chimenti, eds. (Plenum, NY 1987), p. 449-457.
26. W. A. Ellingson, J. L. Ackerman, J. D. Weyand, and R. A. DiMilia, Characterization of Porosity in Green-State and Partially Densified  $Al_2O_3$  by Nuclear Magnetic Resonance Imaging, *Ceram. Eng. Sci. Proc.* 8(7-8), 503-512 (1987).
27. G. C. Chingas, J. B. Miller, and A. N. Garroway, NMR Images of Solids, *J. Magn. Reson.* 66(3), 530-5 (1986).
28. J. B. Miller and A. N. Garroway, Removal of Static Field Inhomogeneity and Chemical-Shift Effects in NMR Imaging, *J. Magn. Reson.* 67, 575 (1986).
29. J. B. Miller and A. N. Garroway, NMR Imaging of Solids, in Review of Progress in Quantitative Nondestructive Evaluation, vol. 7A, eds. Donald O. Thompson and Dale E. Chimenti (Plenum, NY 1988), p. 287-294.
30. J. B. Miller and A. N. Garroway, NMR Imaging of Solids with a Surface Coil, *J. Magn. Reson.* 77, 187-191 (1988)
31. J. B. Miller and A. N. Garroway,  $^1H$  and  $^{13}C$  Refocused Gradient Imaging of Solids, 29th Experimental Nuclear Magnetic Resonance Conf., Rochester, NY, April 17-21, 1988, Poster 144.
32. J. B. Miller and A. N. Garroway,  $^1H$ -Refocused Gradient Imaging of Solids, *J. Magn. Reson.* 82 (accepted, 1989).
33. J. B. Miller and A. N. Garroway, Dipolar Decoupled Inversion Pulses for NMR Imaging of Solids, 30th Experimental Nuclear Magnetic Resonance Conf., Asilomar, CA, April 2-6, 1989, Poster M42.
34. J. M. Listerud, S. W. Sinton, and G. P. Drobny, NMR Imaging of Materials, *Anal. Chem.* 61(1), 23A-41A (1988).
35. J. B. Aguayo, S. J. Blackband, J. Schoeniger, M. A. Mattingly and M. Hintermann, Nuclear Magnetic Resonance Imaging of a Single Cell, *Nature* 322, 190-1 (1986).

36. Doty Scientific, Bruker Instruments, GE NMR Instruments, and Varian Instruments at 30th Experimental Nuclear Magnetic Resonance Conf., Asilomar, CA, April 2-6, 1989.
37. C. Chang and R. A. Komoroski, NMR Imaging of Elastomeric Materials, *Macromolecules* **22**, 600-607 (1989).
38. S. Matsui and H. Kohn, NMR Imaging with a Rotary Field Gradient, *J. Magn. Reson.* **70**, 157-162 (1986).
39. D. G. Cory, A. M. Reichwein, J. W. M. van Os and W. S. Veeman, NMR Images of Rigid Solids, *Chem. Phys. Lett.* **143**(5), 467-470 (1988).
40. D. G. Cory, J. W. M. van Os and W. S. Veeman, NMR Images of Rotating Solids, *J. Magn. Reson.* **76**, 543-547 (1988).
41. D. G. Cory, A. M. Reichwein and W. S. Veeman, Removal of Chemical-Shift Effects in NMR Imaging, *J. Magn. Reson.* **80**, 259-267 (1988).
42. D. G. Cory, J. C. de Boer and W. S. Veeman, Magic Angle Spinning  $^1\text{H}$  NMR Imaging of Polybutadiene/Polystyrene Blends, *Macromolecules* **22**, 1618-1621 (1989).
43. D. G. Cory, New Approaches to NMR Imaging in a Rotating Field Gradient, *J. Magn. Reson.* **82**, 337-341 (1989).
44. D. G. Cory and W. S. Veeman, Magnetic Field Gradient Imperfections in NMR Imaging of Rotating Solids, *J. Magn. Reson.* **82**, 374-381 (1989).
45. C. G. Fry and A. C. Lind, Multiple-Pulse Decoupling and Spin-Echo NMR Imaging of  $^1\text{H}$  in Solids, in preparation.
46. C. G. Fry and A. C. Lind, Nuclear Magnetic Resonance Imaging of Solid Polymeric Materials, *Bull. Am. Phys. Soc.* **34**(3), 759 (1989).
47. A. Abragam, The Principles of Nuclear Magnetism (Clarendon, Oxford, 1961).
48. M. Mehring, Principles of High Resolution NMR in Solids 2nd ed. (Springer-Verlag, NY, 1983).
49. U. Haeberlen, High Resolution NMR in Solids; Selective Averaging, *Adv. Magn. Reson.*, Supplement 1, ed. J. S. Waugh (Academic, NY, 1976).
50. G. A. Johnson, Magnetic Resonance Microscopy, *Bull. Am. Phys. Soc.* **34**(3), 445 (1989).
51. K. R. Carduner, R. O. Carter III, M. E. Milberg, and G. M. Crosbie, Determination of Phase Composition of Silicon Nitride Powders by

Silicon-29 Magic Angle Spinning Nuclear Magnetic Resonance Spectroscopy, Anal. Chem. 59, 2794-2797 (1987).

52. J. B. Miller and A. N. Garroway, private communication.
53. G. H. Glover, C. E. Hayes, N. J. Pelc, W. A. Edelstein, O. M. Mueller, H. R. Hart, C. J. Hardy, M. O'Donnell, and W. D. Barber, Comparison of Linear and Circular Polarization for Magnetic Resonance Imaging, J. Magn. Reson. 64, 255 (1985).
54. R. W. Brown, E. M. Haacke, M. A. Martens, J. L. Patrick, and F. R. Zypman, A Layer Model for RF Penetration, Heating, and Screening in NMR, J. Magn. Reson. 80, 225 (1988).
55. D. G. Gadian and F. N. H. Robinson, Radiofrequency Losses in NMR Experiments on Electrically Conducting Samples, J. Magn. Reson. 34, 449 (1979).
56. A. C. Lind and T. R. Wenger, Measurement of the Complex Dielectric Constant of Lossy Fibers and Rods at Microwave Frequencies, Rev. Sci. Instrum. 58, 844, (1987).
57. L. D. Landau and E. M. Lifshitz, Electrodynamics of Continuous Media (Addison-Wesley, 1960) p 190.
58. R. F. Harrington, Time-Harmonic Electromagnetic Fields (McGraw-Hill, New York 1961) p. 50.
59. F. C. Cambell, A. R. Mallow, K. C. Amuedo, and G. A. Blase, Computer-Aided Curing of Composites, Fifth Quarterly Interim Technical Report, July 1985, USAF Manufacturing Science Program (Contract No. F33615-83-C-5088).
60. R. W. P. King, R. B. Marsh, S. S. Sandler, Arrays of Cylindrical Dipoles (Cambridge University Press, 1968), p. 377.
61. C. E. Hayes, W. A. Edelstein, J. F. Schenck, O. M. Mueller and M. Eash, An Efficient, Highly Homogeneous Radio-Frequency Coil for Whole-Body NMR Imaging at 1.5 T, J. Magn. Reson. 63, 622-628 (1985).
62. R. R. Ernst, G. Bodenhausen, and A. Wokaum, Principles of Nuclear Magnetic Resonance in One and Two Dimensions, Internat. Series of Monographs on Chemistry 14 (Clarendon Press, Oxford 1987) Chap. 10.
63. A. Nieminen and J. Koenig, NMR Imaging of Adhesive Bond Formation, 1988 Bruker NMR User's Conference, Oct. 17-18, 1988, Lowell, MA.

64. J. E. Wertz and J. R. Bolton, Electron Spin Resonance: Elementary Theory and Practical Applications (McGraw-Hill, NY, 1972) p. 460.
65. J. A. Ripmeester, Nuclear Shielding of Trapped Xenon Obtained by Proton-Enhanced, Magic-Angle Spinning  $^{129}\text{Xe}$  NMR Spectroscopy, *J. Am. Chem. Soc.* **104**, 289-290 (1982).
66. E. W. Scharpf, R. W. Crecely, B. C. Gates, and C. Dybowski, Characterization of NiNa-Y Zeolite by Xe-129 NMR Spectroscopy, *J. Phys. Chem.* **90**, 9-11 (1986).
67. T. R. Stengle and K. L. Williamson, NMR Study of Xenon Absorbed Within Solid Polymers: A New Probe of the Amorphous State, *Bull. Am. Phys. Soc.* **32**(3), 613 (1987).
68. T. R. Stengle and K. L. Williamson, Nuclear Magnetic Resonance of Xenon Absorbed in Solid Polymers: A Probe of the Amorphous State, *Macromolecules* **20**, 1428-1430 (1987).
69. B. Shizgal, Calculation of the NMR Relaxation Time of Dilute  $^{129}\text{Xe}$  Gas, *Chem. Phys.* **5**, 464-470 (1974).
70. M. D. Sefcik, J. Schaefer, J. A. E. Desa, and W. B. Yelon, Effects of Sorbed Gases on the Molecular Dynamics and Structure of Glassy Polymers, *Polym. Prepr. (Am. Chem. Soc., Dev. Polym. Chem.)* **24**(1), 85-86 (1983).
71. P. T. Inglefield, 30th Experimental Nuclear Magnetic Resonance Conf., Asilomar CA, April 1989, Poster M88, and private communications.
72. B. C. Gerstein and C. R. Dybowski, Transient Techniques in NMR of Solids: An Introduction to Theory and Practice (Academic, NY, 1985).
73. T. M. Duncan,  $^{13}\text{C}$  Chemical Shieldings in Solids, *J. Phys. Chem. Ref. Data* **16**(1), 125-151 (1987).
74. T. C. Farrar and E. D. Becker, Pulse and Fourier Transform NMR (Academic, NY, 1971), p. 39.
75. E. O. Brigham, The Fast Fourier Transform (Prentice-Hall, Englewood Cliffs, NJ, 1974).
76. Y.-S. Yen and A. Pines, Multiple-Quantum NMR in Solids: Part II, *J. Chem. Phys.* **78**(6), 3579 (1983).
77. C. E. Bronnimann, B. L. Hawkins, M. Zhang, and G. E. Maciel, Combined Rotation and Multiple Pulse Spectroscopy as an Analytical Proton

Nuclear Magnetic Resonance Technique for Solids, Anal. Chem. 60, 1743-1750 (1988).

78. C. Dybowski and R. G. Pembleton, Dipolar Narrowed Carr-Purcell Measurement of Rotating Frame Spin-Lattice Parameters in Polymers, J. Chem. Phys. 70(4), 1062 (1979).
79. C. G. Fry and A. C. Lind, A Quadrature Detection Scheme for the BR-24 Pulse Sequence, in preparation.
80. W. K. Rhim, D. P. Burum and R. W. Vaughan, Extraction of Quadrature Phase Information From Multiple Pulse NMR Signals, Rev. Sci. Instrum. 47(7), 720-5 (1976).
81. A. A. Samoililenko, D. Y. Artemov and L. A. Sibeldina, Application of NMR Imaging to the investigation of the Solid State, Bruker Report 2, 30-31, (1987), Bruker Instrum., Inc., Billerica, MA.
82. R. Kimmich and R. Bachus, NMR Field-Cycling Relaxation Spectroscopy, Transverse NMR Relaxation, Self-Diffusion and Zero-Shear Viscosity: Defect Diffusion and Reptation in Nonglassy Amorphous Polymers, Colloid & Polymer Sci. 260, 911-936 (1982).
83. L. J. Friedman, A. K. M. Weenberg, S. N. Ytterboe, and H. M. Bozler, Direct Detection of Low-Frequency NMR Using a DC SQUID, Rev. Sci. Instrum. 57(3), 410-413 (1986)
84. R. A. Webb, New Technique for Improved Low-Temperature SQUID NMR Measurements, Rev. Sci. Instrum. 48(12), 1585-1594 (1977)
85. J. Clarke and R. H. Koch, The Impact of High-Temperature Superconductivity on SQUID Magnetometers, Science 242, 217-223 (1988).
86. E. Fukushima and S. B. W. Roeder, Experimental Pulse NMR: A Nuts and Bolts Approach (Addison-Wesley, Reading, MA, 1981).
87. W. G. Clark, Pulsed Nuclear Resonance Apparatus, Rev. Sci. Instrum. 35(3), 316 (1964).